



Light-induced deformation and instability of a liquid interface. II. Dynamics

Régis Wunenburger, Alexis Casner, Jean-Pierre Delville

► To cite this version:

Régis Wunenburger, Alexis Casner, Jean-Pierre Delville. Light-induced deformation and instability of a liquid interface. II. Dynamics. *Physical Review E: Statistical, Nonlinear, and Soft Matter Physics* [2001-2015], 2006, 73 (3), pp.036315 (1-14). [⟨10.1103/PhysRevE.73.036315⟩](#). [⟨hal-00389845⟩](#)

HAL Id: hal-00389845

<https://hal.science/hal-00389845v1>

Submitted on 29 May 2009

HAL is a multi-disciplinary open access archive for the deposit and dissemination of scientific research documents, whether they are published or not. The documents may come from teaching and research institutions in France or abroad, or from public or private research centers.

L'archive ouverte pluridisciplinaire **HAL**, est destinée au dépôt et à la diffusion de documents scientifiques de niveau recherche, publiés ou non, émanant des établissements d'enseignement et de recherche français ou étrangers, des laboratoires publics ou privés.



HAL Authorization

Light induced deformation and instability of a liquid interface -

II. Dynamics.

Régis Wunenburger,^{*} Alexis Casner,[†] and Jean-Pierre Delville[‡]

*Centre de Physique Moléculaire Optique et Hertzienne, Université Bordeaux I,
351 cours de la Libération, 33405 Talence Cedex, France*

Abstract

We study the dynamics of the deformation of a soft liquid-liquid interface by the optical radiation pressure of a focused cw gaussian laser beam. We measured the temporal evolution of both the hump height and the hump curvature by direct observation and by detecting the focusing effect of the hump acting as a lens. Extending the results of Yoshitake *et al.* [J. Appl. Phys. **97**, 024901 (2005)] to the case of liquid-liquid interfaces and to the $Bo \simeq 1$ regime ($Bo = (\omega_0/\ell_c)^2$, where ω_0 is the beam waist and ℓ_c the capillary length), we show that, in the $Bo \ll 1$ and $Bo \simeq 1$ ranges, the small amplitude deformations are correctly described by a linear hydrodynamic theory predicting an overdamped dynamics. We also study the dynamics of the large amplitude interface deformations at the onset of the opto-hydrodynamic instability [Phys. Rev. Lett. **90**, 144503 (2003)]. Using a simple, phenomenological model for the nonlinear evolution of the hump height, we interpret the observed interface dynamics at the instability onset as the signature of an imperfect subcritical instability.

PACS numbers: 47.20.Ma 42.50.Vk 68.05.-n 68.03.Kn

^{*}Electronic-mail: r.wunenburger@cpmoh.u-bordeaux1.fr

[†]Present address: Département de Conception et de Réalisation d'Expériences, CEA/DAM Ile-de-France, BP 12, F-91680 Bruyères-le-Châtel, France; Electronic-mail: alexis.casner@cea.fr

[‡]Electronic-mail: jp.delville@cpmoh.u-bordeaux1.fr

I. INTRODUCTION

First attempts at observation of measurable liquid interface deformations by laser waves were performed with fairly high energy laser pulses [1–3] because the transfer of photon momentum to a dielectric interface is intrinsically weak and the corresponding pressure, which is proportional to the index contrast and the beam intensity, pushes against the Laplace pressure associated to interfacial tension. For example, Ashkin and Dziedzic [1] performed an experiment using a frequency doubled Nd:Yag laser (wavelength in vacuum $\lambda_0 = 0.53\mu m$) strongly focused on the water free-surface (beam waist value $\omega_0 = 2.1\mu m$). Due to the large value of the water/air surface tension ($\sigma = 73mJ.m^{-2}$), they worked with laser pulses (pulse duration $60ns$ and peak power between 1 and $4kW$) to increase radiation pressure effects by compensating the weakness of the index contrast by the beam intensity. The interface bending was still very weak (typically a few hundreds of nanometers in height). Similarly, to observe interface disruption, Zhang and Chang [2] considered the incident radiation from a flashlamp-pumped dye laser emitting at $\lambda = 0.6\mu m$ with a spot diameter of $\sim 200\mu m$, a pulse duration of $400ns$ and an energy varying between 100 and $200mJ$. Both examples raised an important property of radiation pressure effects. With classical fluids, the time scale associated to the growth rate of the interface deformation is of the order of a few hundreds of nanoseconds (typically $400ns$ and $4\mu s$, respectively for the Ashkin-Dziedzic and the Zhang-Chang conditions). Since interface deformation also means lensing [1, 4], these experiments strongly suggest the way to build adaptive optical blocks with fast switching response such as microlenses. That is why radiation pressure effects produced by pulsed lasers were extended to the recording of dynamic holograms [3]. Compared to thermally-driven surface relief distortions caused by surface tension gradients (also called Marangoni or thermo-capillary deformations [5, 6]), which are used for infrared imaging [7] and hologram writing too [8], non thermal deformations produced by the radiation pressure have two main advantages: (i) energy is not dissipated and, (ii) the recording and the erasure rate are not determined by mass and thermal transport over the entire fluid layer (i.e. the rates do not depend on the thickness of the sample). However, even if all these experiments clearly illustrate the potentialities of radiation pressure effects in terms of adaptive optical addressing, they present a major drawback. The high radiation intensities needed to noticeably deform interfaces require reasonably short pulses, typically less or of the order of a few hundreds of

nanosecond as in the experiments presented above. Consequently, the response time of the fluid interface is always much longer than the pulse duration. This prevents investigations of the entire dynamics of a fully developed deformation; this dynamics is always truncated. Moreover, to reach high beam intensities, Q-switched laser were commonly used. The resulting amplification of the irradiance leads to pulses of complex shape which are difficult to characterize while the spatio-temporal profile of the wave is crucial for the calculation of the radiation pressure and the resulting interface deformation. That is why recent investigations on interface deformations by the radiation pressure considered instead continuous laser waves which were further modulated temporally. The main drawback is that interface deformations become too weak to be directly observed. This is certainly the reason why so few works were dedicated to radiation pressure, even if the Ashkin's adaptive lensing method offers sufficiently valuable sensitivity for the detection of the induced nanometric bulge and further quantitative measurements. However, the eighties have seen the emergence of the so-called soft matter physics that brought a sort of renewal to laser radiation pressure by opening new horizons beyond the optical physics area. For example, Sakai *et al.* [9] showed how periodic radiation pressure can control the excitation of capillary waves and how the characterization of their dynamics can be used to deduce surface or bulk properties such as surface tension and low amplitude shear viscosities. The key point here is the contactless property of the method which allows for in situ measurements and prevents mechanical contact with fluid surfaces as well as possible chemical contamination by these mechanical disturbances. This dynamical approach was further extended to the difficult problem of the quantitative measurements of high viscosity systems [10]. The advantage here is the rapidity of measurements (typically a few seconds) associated to the fact that the viscous motion of the fluid is limited to the microscopic volume excited by the laser beam.

Improvements in these applications, for instance, require an experimental confrontation to the different dynamic regimes that are expected to depend on the competition between capillary waves, and overdamped modes resulting from viscous dissipation. While now the efficiency of the technique is well established in several conditions, the demonstration of its versatility still deserves further developments because it appears several regimes in interface deformation that have not been studied yet. For example, buoyancy effects were neglected in the experiments presented above. If such an assumption is realistic for usual fluids, for which the surface tension of the free-surface is generally large, it is not necessarily true

when surfactants are present at the interface between two fluids as in soft materials. As illustrated in the following, the equation describing the dynamics of laser-induced interface deformations includes both properties of the used fluids (the density contrast at the interface in the hydrostatic pressure term, the surface tension in the Laplace pressure and the shear viscosity in the dynamic viscous pressure) and external optical parameters, such as the beam power and the beam waist. This gives us the opportunity to build new dimensionless quantities, such as an optical Bond number Bo which takes into account the coupling and the competition between the characteristic length scale of the optical excitation and that of the fluid interface. We showed that stationary deformations can be described by a universal function of Bo [11]. This function presents two asymptotic regimes. Depending on whether $Bo \ll 1$ (case of usual fluids) or $Bo \gg 1$ (when surface tension effects are dominated by buoyancy), we showed in the preceding companion article [12] that stationary deformations are described by different universal behaviors.

In the present investigation, we extend this approach to the description of the dynamics of interface deformations driven by the radiation pressure. Moreover, beyond our analysis of the linear regime (deformations of small amplitude) in terms of scaled behavior, our knowledge on non-linear interface deformations, which appear at high laser irradiance, is scarce. Since the publication, more than fifteen years ago by Zhang and Chang [2], of impressive pictures of the dynamics of droplets disruption driven by laser pulses, almost nothing has been presented in this direction, except three theoretical descriptions of the weakly non-linear regime of deformation [13–15]. Based on linear wave theory, they cannot nevertheless explain giant deformations as well as the subsequent droplet disruption. In the preceding companion article [12], devoted to the investigation of stationary behaviors, we showed that deformations of large amplitude may become unstable above a beam power threshold, leading to the formation of a long beam centered jet. We also proposed an instability mechanism based on total reflection of light within the induced deformation. From the fundamental point of view, the investigation of the corresponding dynamics would obviously bring new insights on the mechanism of this "opto-hydrodynamic" instability which illustrates subtle nonlinear couplings between laser propagation and interface deformation. As the instability leads to the formation of liquid microjets, this is also of practical interest for the development of optically-driven applications analogous to electro-spraying [16] or ink-jet printing [17].

Our aims are thus the following: (i) to identify the characteristic timescales of the interface motion in the linear regime, (ii) to evidence a slow dynamics just beyond the instability threshold that is characteristic of a subcritical instability, (iii) to study whether the interface dynamics at instability onset is compatible with our model of total internal reflection induced instability. In Sec. II, we summarize the main results of the preceding companion article [12] that constitute the indispensable background to the present study of the dynamics of interface deformations. Sec. III is dedicated to the theoretical description of the linear dynamics of the interface when suddenly submitted to the radiation pressure of a gaussian cw laser beam. In Sec. IV, we present our measurements of the characteristic timescale of the overdamped hump height and curvature dynamics for small amplitude interface deformations, and compare them to the prediction of the linear theory. Finally, in Sec. V we model our measurements of the interface dynamics at instability onset, and link them to the model of total internal reflection induced instability.

II. OVERVIEW ON STEADY LASER-DRIVEN INTERFACE DISTORTION

Let us assume a liquid interface intercepted by a continuous laser wave propagating vertically along the z -axis. The amplitude of the resulting steady distortion $h(r)$ of the flat liquid surface induced by the optical radiation pressure depends on the combined effect of gravity and surface tension. At steady state, the equation of motion for the height $h(r)$, where r is the radius in cylindrical coordinates, is given by [12]:

$$(\rho_1 - \rho_2)gh(r) - \frac{\sigma}{r} \frac{\partial}{\partial r} \left(\frac{rh'(r)}{\sqrt{1 + h'(r)^2}} \right) = \Pi(r, \theta_i), \quad (1)$$

where ρ_1 and ρ_2 are the densities of the two superposed liquids, σ is the surface tension, and $\Pi(r, \theta_i)$ is the optical radiation pressure for an incidence angle θ_i . In the linear regime of deformation, one has $|h'(r)| \ll 1$ and the value of the radiation pressure can be taken at normal incidence ($\theta_i = 0$) (see, for instance, Eq. (9) of Ref. [12]). Then, for an exciting beam in the TEM_{00} mode, the solution for $h(r)$ can be calculated by use of a Fourier-Bessel, or Hankel, transform. However, by comparing the relative effect of the hydrostatic pressure (buoyancy) with that of the Laplace pressure (surface tension), one can define an optical Bond number as $Bo = (\omega_0/\ell_c)^2$, where ω_0 is the beam waist of the exciting beam and $\ell_c = \sqrt{\sigma/g(\rho_1 - \rho_2)}$ is the capillary length associated to the interface. When $Bo \ll 1$,

gravity turns out to be negligible for the surface distortion. The height of the deformation is in this case inversely proportional to the surface tension σ and is thus considerably enhanced when σ is small. That is why our experiments are performed in a water-in-oil microemulsion (stable suspension of surfactant-coated water nanodroplets, called micelles, dispersed in an oil-rich continuum). The composition and some of the characteristics of the chosen microemulsion have already been described [12]. For a temperature $T > T_c$, where $T_c = 308K$ is a critical temperature, the mixture separates in two micellar phases, ϕ_1 and ϕ_2 , of different micellar concentrations. As the density (resp. index of refraction) of water is larger (resp. smaller) than that of oil, the micellar phase ϕ_1 with the larger concentration is located below the low micellar concentration phase, ϕ_2 , whereas its refractive index n_1 is smaller than n_2 of ϕ_2 . The main advantages of this type of medium are (i) the intrinsically weak surface tension of the liquid meniscus separating the two phases (due to the presence of surfactant molecules) and (ii) the ability to even reduce this surface tension by approaching the critical point (typically 10^6 times smaller at $T - T_c = 3K$ than that of the water-air free surface). Low residual optical absorption at the used wavelength are also required to prevent disturbing thermal heating. This last condition is fulfilled for our micellar phases since the optical linear absorption is $\alpha_0 = 3.10^{-4}cm^{-1}$. As a consequence, continuous laser waves can easily monitor interface deformations without inducing thermal coupling or optical bulk nonlinearity. On the other hand, the vicinity of a critical point ensures the universality of the observed phenomena, because our mixture belongs to the universality class ($d = 3, n = 1$) of the Ising model [18]. Critical universality also allows us to evaluate the experimental parameters of our system according to the following universal scaling laws for surface tension and the density contrast between the two phases: $\sigma = \sigma_0 \left(\frac{T-T_c}{T_c} \right)^{2\nu}$, with $\nu = 0.63$ and $\sigma_0 = 10^{-4}J.m^{-2}$; $\Delta\rho = \rho_1 - \rho_2 = \Delta\rho_0 \left(\frac{T-T_c}{T_c} \right)^\beta$ with $\beta = 0.325$ and $\Delta\rho_0 = 284kg.m^{-3}$. Since the two phases ϕ_1 and ϕ_2 are of similar composition, we assumed the Clausius-Mossotti relation $\Delta n \approx (\partial n / \partial \rho)_T \Delta\rho$, to be valid for the refractive-index contrast $\Delta n = n_1 - n_2$, with $(\partial n / \partial \rho)_T = -1.22.10^{-4}m^3.kg^{-1}$.

The experimental setup is well described in Ref. [12]. The mixture is enclosed in a thermoregulated spectroscopic cell, and the temperature is chosen above T_c to reach the two-phase equilibrium state. The bending of the liquid-liquid meniscus is driven by a linearly polarized TEM_{00} cw Ar^+ laser (wavelength in vacuum $\lambda_0 = 514.5nm$) propagating either upward or downward along the vertical axis. The beam is focused on the interface by a

microscope objective (Leitz; 10 \times ; N.A., 0.25). In what follows, P is the beam power and we adjust the beam waist ω_0 , evaluated at $1/e^2$, by changing the distance between a lens (focal length, $f = 0.3m$, resp. $1m$, for upward, resp. downward, excitation) and the focusing objective. Interface deformations are illuminated by a white light source and observed using a standard or a high speed CCD video camera.

Typical interface deformations induced at $T - T_c = 3K$ and $\omega_0 = 5.3\mu m$ are presented in Fig. 1 for both upward- and downward directed beams. As $n_1 < n_2$, the radiation pressure acts downward toward the less-refractive medium, regardless of the direction of propagation of the laser [12]. Fig. 1 also shows the variation of the height $h(r = 0)$ versus beam power P in both cases. As expected and already discussed [12], $h(r = 0)$ is proportional to P at low beam power. In the presented example, this regime corresponds to $P \leq 225mW$ and $P \leq 300mW$, respectively for upward and downward beam excitation. With further increase in P , $h(r = 0)$ gradually deviates from linearity. The deformation switches from the classic bell shape to a stable tether shape in the upward-directed case; see the three last pictures at the bottom of Fig. 1. The behavior is radically different for downward excitation. The deformation suddenly loses stability, and diverges above a well-defined threshold power $P = P_\dagger = 400mW$ (see the second picture on top of Fig. 1) which corresponds to the instability onset. This instability gives birth to a stationary liquid jet emitting droplets; see the first picture on top of Fig. 1. Self-trapping of the beam by the jet is also clearly evidenced. More insights on the underlying physics can be found from the investigation of the interface dynamics leading to these stationary regimes of deformation. This is the purpose of the next section, where the theoretical background required to analyze experimental data is presented.

III. THEORY OF THE INTERFACE LINEAR DYNAMICS

A. Basic linear model

The dynamics of a small amplitude deformation of the free surface of a liquid of density ρ and refractive index n when submitted to the electromagnetic radiation pressure of a laser beam was theoretically described first by Ostrovskaya [19]. This dynamics was analyzed by solving the unsteady, linearized Navier-Stokes and mass conservation equations in cylindri-

cal coordinates with the linearized boundary condition at the free surface detailed in the following. In the unsteady linear model, the small amplitude deformations hypothesis allows to linearize the pressure continuity condition at the free surface in the same manner as Eq. (9) of the first companion article [12]:

$$\rho gh(r, t) - \sigma \frac{1}{r} \frac{d}{dr} (rh'(r, t)) - 2\eta \frac{\partial v_z}{\partial z}(r, t) = \Pi(r, t, \theta_i(r, t) = 0), \quad (2)$$

where $\eta = \rho\nu$ is the liquid dynamic viscosity, $v_z(r, t)$ is the vertical velocity field of the liquid, and

$$\Pi(r, t, \theta_i(r, t) = 0) = \frac{2P}{\pi\omega_0^2 c} \frac{2n(n-1)}{n+1} e^{-\frac{r^2}{2\omega_0^2}} H(t) \quad (3)$$

is the radiation pressure field acting on the free surface at normal incidence. We assume interface excitation by a cylindrical gaussian beam of waist ω_0 and power P , switched on at time $t = 0$ (H is the Heaviside function). This linear set of equations was solved using Hankel transform \mathfrak{H} with respect to coordinate r , defined as $\mathfrak{H}\{f\}(k) = \int_0^{+\infty} r J_0(kr) f(r) dr$ and Laplace transform \mathfrak{L} with respect to time, defined as $\mathfrak{L}\{g\}(s) = \int_0^{+\infty} e^{-st} g(t) dt$. The evolution of the surface deformation is finally obtained using the approximation: $h(r, t) \simeq \int_0^t v_z(r, z = 0, t') dt'$ with:

$$v_z(r, z = 0, t) = \frac{P}{\pi c \eta} \frac{n(n-1)}{n+1} \int_0^{+\infty} \frac{J_0(kr) e^{-\frac{k^2 \omega_0^2}{8}}}{\nu k^2} \mathfrak{L}^{-1} \left\{ \frac{1}{(A^2(k, s) + 1)^2 - 4A(k, s) + \Delta(k)} \right\} dk, \quad (4)$$

where

$$A^2(k, s) = 1 + \frac{s}{\nu k^2}, \quad (5)$$

$$\Delta(k) = \frac{gk + \frac{\sigma k^3}{\rho}}{(\nu k^2)^2}. \quad (6)$$

Since $\mathfrak{L}^{-1} \left\{ \frac{1}{f(s)} \right\} (t) = \sum_i \frac{e^{s_i t}}{f'(s_i)}$ when the function $f(s)$ has only simple, isolated poles s_i [20], the timescales of the motion of a deformation characterized by the wave number k are the roots of the denominator of the last term of the integrand in Eq. (4), which is precisely the dispersion relation for plane surface waves of wave number k at a free surface of a viscous liquid [21]. The physically acceptable roots of the dispersion relation have to support $Re(A^2(k, s)) \geq 0$ in order to satisfy the boundary condition $v_z(r, z, t) \xrightarrow{z \rightarrow -\infty} 0$ [19, 22].

B. Characteristic timescales obtained from the dispersion relation

The one-fluid model can be adapted to the interface between two liquids 1 and 2 by applying to Eqs. (4-6) the following transformations [23]: $\rho \leftrightarrow \rho_1 + \rho_2$, $gk + \frac{\sigma k^3}{\rho} \leftrightarrow \frac{\rho_1 - \rho_2}{\rho_1 + \rho_2} gk + \frac{\sigma}{\rho_1 + \rho_2} k^3$, $\eta \leftrightarrow \eta_1 + \eta_2$. Thus, a realistic order of magnitude of the characteristic timescales of evolution of the interface deformations observed in our experiment should be obtained by solving the dispersion relation of interfacial viscous waves of wave number k :

$$\left(s + 2 \frac{\eta_1 + \eta_2}{\rho_1 + \rho_2} k^2 \right)^2 + \Omega(k)^2 = 4 \left(\frac{\eta_1 + \eta_2}{\rho_1 + \rho_2} k^2 \right)^2 \sqrt{1 + \frac{s}{\frac{\eta_1 + \eta_2}{\rho_1 + \rho_2} k^2}}, \quad (7)$$

$$\Omega(k)^2 = \frac{\rho_1 - \rho_2}{\rho_1 + \rho_2} gk + \frac{\sigma}{\rho_1 + \rho_2} k^3, \quad (8)$$

with $Re \left(1 + s \left(\frac{\eta_1 + \eta_2}{\rho_1 + \rho_2} k^2 \right)^{-1} \right) \geq 0$. As the interface is excited by a laser beam of waist ω_0 , we assume the characteristic length scale of interface deformation to be ω_0 , i.e. $k \simeq \omega_0^{-1}$.

This dispersion relation is often handled for “low viscosity” liquids, i.e. for $\Omega(k) \gg \frac{\eta_1 + \eta_2}{\rho_1 + \rho_2} k^2$, resulting in propagative damped gravitational-capillary waves of approximate pulsation $\Omega(k)$ and damping timescale $(2 \frac{\eta_1 + \eta_2}{\rho_1 + \rho_2} k^2)^{-1}$ [9, 19]. Given the small values of $\omega_0 \sim 10^{-5}$ m, of $\sigma \sim 10^{-7} J.m^{-1}$, and of $\rho_1 - \rho_2 \sim 50 kg.m^{-3}$ encountered in our experiments, and given $\rho_1 \simeq \rho_2 \sim 1000 kg.m^{-3}$, $\eta_1 \simeq \eta_2 \simeq \langle \eta \rangle \sim 10^{-3} kg.m^{-1}.s^{-1}$, we find instead $\Omega(k) \ll \frac{\eta_1 + \eta_2}{\rho_1 + \rho_2} k^2$. Thus, the interface dynamics falls in the so-called regime of overdamped surface waves [24, 25]. In the $\Omega(k) \ll \frac{\eta_1 + \eta_2}{\rho_1 + \rho_2} k^2$ limit, Eq. (7) has (i) two complex, conjugate roots $s_{1,2}(k) \simeq \frac{\eta_1 + \eta_2}{\rho_1 + \rho_2} k^2 (-1.77 \pm 1.11i)$ that are to be rejected since $Re(A^2(k, s_{1,2})) < 0$ and (ii) two real roots $s_3(k) \simeq -0.91 \frac{\eta_1 + \eta_2}{\rho_1 + \rho_2} k^2$ and $s_4 \simeq -\Omega(k)^2 \left(2 \frac{\eta_1 + \eta_2}{\rho_1 + \rho_2} k^2 \right)^{-1}$ [21]. Consequently, the interface motion is not oscillatory but just damped. Finally, assuming $k \simeq \omega_0^{-1}$, we find $s_3 \simeq 10^5 s^{-1}$ and $s_4 \simeq 10^2 s^{-1}$, i.e. $|s_4| \ll |s_3|$ in our experimental conditions. Consequently, the interface motion characterized by s_3 , corresponding to the viscous diffusion of momentum over the length scale ω_0 , is damped very rapidly, and the interface motion should be mainly damped on the timescale $\tau = -s_4^{-1}$ which can be expressed as:

$$\tau(k) = \frac{2(\eta_1 + \eta_2)k^2}{(\rho_1 + \rho_2)\Omega(k)^2} \simeq \frac{4\langle \eta \rangle}{\sigma k} (1 + (k\ell_c)^{-2})^{-1}. \quad (9)$$

Using $k = \omega_0^{-1}$, τ can be written as

$$\tau(\omega_0^{-1}) \simeq \frac{4\langle \eta \rangle \omega_0}{\sigma} (1 + Bo)^{-1}, \quad (10)$$

with $\frac{\eta_1+\eta_2}{2} \simeq \langle \eta \rangle = 1.27 \cdot 10^{-3} \text{ Pa.s}$ [26], $\frac{\rho_1+\rho_2}{2} \simeq \langle \rho \rangle = 871.6 \text{ kg.m}^{-3}$. The dispersion relation of the plane interfacial waves predicts that the characteristic timescale of the hump relaxation should scale as $\tau(\omega_0^{-1}) = \tau_0 = \frac{4\langle \eta \rangle \omega_0}{\sigma}$ in the $Bo \ll 1$ regime, and as $\tau(\omega_0^{-1}) = \tau_\infty = \frac{4\langle \eta \rangle}{g\omega_0 \Delta \rho}$ in the $Bo \gg 1$ regime.

C. Overdamped dynamics of the hump height and curvature

As we measured the dynamics of both the hump height $h(0, t)$ and the hump curvature $\kappa(0, t) = \frac{1}{r} \frac{d}{dr} \left(r \frac{dh}{dr} \right) (0, t)$ in the $Bo \ll 1$ and $Bo \simeq 1$ regimes, here we study numerically the actual behavior of these quantities with respect to the Bo number. The major concern of this Section is to determine whether the predictions for the characteristic timescale for the dynamics of both the hump height and curvature obtained from the dispersion relation of plane interfacial waves are realistic in the case of an axisymmetric deformation induced by a gaussian laser beam.

Using the physically acceptable roots of the dispersion relation presented in the last section, and neglecting the rapidly damped motion characterized by s_3 , we can transform and integrate Eq. (4) to get :

$$h(0, t) \simeq -\frac{\Pi_0 \omega_0^2}{2(\rho_1 + \rho_2)} \int_0^\infty \frac{k^2}{\Omega(k)^2} e^{-\frac{k^2 \omega_0^2}{8}} (1 - e^{s_4(k)t}) dk, \quad (11)$$

and

$$\kappa(0, t) \simeq -\frac{\Pi_0 \omega_0^2}{2(\rho_1 + \rho_2)} \int_0^\infty \frac{k^4}{\Omega(k)^2} e^{-\frac{k^2 \omega_0^2}{8}} (1 - e^{s_4(k)t}) dk, \quad (12)$$

after a time long compared to s_3^{-1} . $\Pi_0 = \frac{4Pn_i}{\pi c \omega_0^2} \frac{n_2 - n_1}{n_2 + n_1}$ is the radiation pressure along the beam axis [12], where the index i refers to the incident fluid. Numerical integration of Eqs. (11, 12) is performed using *Matlab*[®]. Since the functional form of the hump height and curvature depend on the Bo value, we choosed to compare the characteristic timescales of their relaxing behavior at any Bo value by fitting the reduced hump height $h^*(t) = h(0, t)/h(0, \infty)$ and the reduced curvature $\kappa^*(t) = \kappa(0, t)/\kappa(0, \infty)$ with a unique, natural, experimentalist-friendly, functional form $1 - e^{-\frac{t}{\tau_{\text{eff}}}}$, with τ_{eff} as free parameter.

1. Hump height behavior

Variations of h^* versus the reduced time $t^* = t/\tau(\omega_0^{-1})$ are plotted in Fig. 2 for several values of Bo , together with their best exponential fit. As predicted by Eq. (7), $h^*(t^*)$ relaxes monotonously up to unity, qualitatively as its exponential fit. But the closer to unity the Bo number, the better the agreement between $h^*(t^*)$ and its best exponential fit. We first consider the behavior of $h^*(t^*)$ without surface tension ($Bo = \infty$), shown in Fig. 2. Its best exponential fit, also shown in Fig. 2, gives $\tau_{\text{eff}} \simeq 2.35 \tau_\infty$. This means that in the $Bo \gg 1$ regime, the prediction of the dispersion relation of interfacial plane waves is realistic, provided that the effective wave number used in the dispersion relation is $k_{\text{eff}} \simeq 2.35 \omega_0^{-1}$.

The variation of the reduced characteristic timescale of relaxation of $h^*(t^*)$, $\tau_{\text{eff}}/\tau(\omega_0^{-1})$ versus Bo is shown in the Inset of Fig. 2. τ_{eff} scales as $\tau_0 Bo^{-1/3}$ as $Bo \rightarrow 0$ ($\tau_{\text{eff}} \simeq 0.47\tau_0 Bo^{-1/3}$ at $Bo \ll 1$). This is linked to the fact that the static hump height becomes infinite at $Bo = 0$, when $g = 0$ or $\omega_0 = 0$ [12, 28]. This divergence of τ_{eff} practically means that there is no Bo independent, effective wave number that makes the prediction of the dispersion relation quantitatively accurate for the dynamics of the hump height in the $Bo \ll 1$ regime.

2. Hump curvature behavior

We first consider the behavior of κ^* versus t^* without gravity ($Bo = 0$), presented in Fig. 3 together with its best exponential fit. As shown in ref. [10],

$$\kappa^*(t^*) \propto t^* e^{2t^{*2}} \text{erfc}(\sqrt{2}t^*). \quad (13)$$

Its best exponential fit gives $\tau_{\text{eff}} \simeq 0.48\tau_0$. This means that in the $Bo \ll 1$ regime, and concerning the dynamics of the hump curvature, the prediction of the dispersion relation of interfacial plane waves is realistic. Furthermore, the effective wave number to be used in the dispersion relation is $k_{\text{eff}} \simeq 2.1\omega_0^{-1}$. We now consider the behavior of $\kappa^*(t^*)$ without surface tension ($Bo = \infty$), shown in Fig. 3. Its best exponential fit gives $\tau_{\text{eff}} \simeq 3.62 \tau_\infty$. This means that in the $Bo \gg 1$ regime, the prediction of the dispersion relation of interfacial plane waves is also realistic. In this case, the effective wave number to be used in the dispersion relation is $k_{\text{eff}} \simeq 3.6 \omega_0^{-1}$.

We finally consider the variations of $\kappa^*(t^*)$, plotted in Fig. 3 for several values of Bo , together with their best exponential fit. The agreement between $\kappa^*(t^*)$ and its best exponential fit is found to be excellent at any Bo value. The variation of the reduced characteristic timescale of relaxation of $\kappa^*(t^*)$, $\tau_{\text{eff}}/\tau(\omega_0^{-1})$ versus Bo is shown in the Inset of Fig. 3. The observed weak variation of $\tau_{\text{eff}}/\tau(\omega_0^{-1})$ over the wide range $Bo = 5 \cdot 10^{-2} - 10^3$ shows that τ_{eff} actually scales as $\tau(\omega_0^{-1})$ both in the $Bo \ll 1$ and $Bo \gg 1$ regimes. Thus, the use of $k = \omega_0^{-1}$ in the dispersion relation of plane interfacial waves gives the right order of magnitude for the characteristic timescale of evolution τ_{eff} of the hump curvature $\kappa(0, t)$ at any Bo value. In particular, $\tau_{\text{eff}} \simeq 0.5\tau(\omega_0^{-1})$ holds up to $Bo \simeq 1$.

To summarize this section, the numerical study demonstrates that (i) the behavior of the hump curvature evolution $\kappa(0, t)$ is closer to an exponential relaxation than the hump height evolution $h(0, t)$ at any Bo value, making exponential fits of experimental hump curvature evolution more pertinent than those of hump height, (ii) the characteristic timescale of evolution of the hump curvature is correctly predicted by the dispersion relation of plane interfacial waves assuming $k = \omega_0^{-1}$ given any value of Bo , whereas the dispersion relation fails in the $Bo \ll 1$ regime in predicting the characteristic timescale of evolution of the hump height.

IV. MEASUREMENT OF THE CHARACTERISTIC TIMESCALE OF THE INTERFACE MOTION

In order to experimentally characterize the timescale of the interface deformation dynamics when it is submitted to the radiation pressure of a laser beam, we proceeded in two ways. At first, we captured the motion of the hump formed at the interface, extracting its height $h(0, t)$ along the beam axis. Then, we used the focusing property of the interface hump [4] in the same way as Sakai et al. [27] to measure the dynamics of the hump curvature along the beam axis $\kappa(0, t)$. We present sequentially our measurements of both the hump height and curvature dynamics, and compare them to their prediction presented above.

3. Hump height dynamics

The experimental setup is described in detail in the preceding companion article [12]. We captured the motion of the interface using a *High Speed MotionMeter Redlake* digital video camera of resolution 292×220 acquiring 250 fps. Then we extracted the hump height along the beam axis $h(0, t)$ from the pictures. We performed these experiments in the temperature range $T - T_C = 5 - 25K$ and for beam waist varying from 5 to $8.9\mu m$, corresponding to a range of Bo number $7.10^{-3} - 0.1$. A typical evolution of the interface distortion against time is shown in Fig. 4.

A series of hump height evolutions is shown in Inset of Fig. 5. In order to be allowed to compare our measurements of τ_{eff} to the linear model presented in Sec. III C 1, experiments have to be performed in the linear regime, i.e. the measured value of τ_{eff} has to be independent of the beam power P . To check this requirement, and simultaneously measure τ_{eff} , we used the procedure illustrated in Fig. 5 for each chosen couple $(\omega_0, T - T_c)$. The temporal behavior of $h(0, t)$ is extracted from image analysis for several beam power values. Then, as explained in Sec. III, the curves are independently fitted with an exponential function in order to get both the asymptotic hump height $h(0, \infty)$ and the relaxation time scale τ_{eff} , as illustrated in the Inset of Fig. 5. The deduced asymptotic hump heights are used to reduce the height $h(0, t)$. An example of data reduction, expected for the linear regime of deformation, is presented in Fig. 5. On the other hand, the measurement of different values of the relaxation time allows the determination of a mean value of τ_{eff} , which must be retrieved from the fit of the full reduced data set.

Since experiments were performed in the $Bo \ll 1$ regime, the effective timescale of exponential relaxation of the hump height, τ_{eff} , is expected to scale as $\tau_0 Bo^{-1/3}$. This means that $\tau_{\text{eff}} \sim \omega_0^{1/3} (T - T_c)^{-0.95}$. Thus, τ_{eff} is expected to increase versus both the beam waist and the vicinity to the critical point. The first expectation is confirmed in Fig. 6, while an example of the second one is given in the Inset.

Finally, the variation of τ_{eff} versus $\frac{4\langle\eta\rangle\omega_0}{\sigma} Bo^{-1/3}$, plotted in Fig. 7, validates this predicted scaling. Moreover, the slope of the best linear fit of the experimental data is 0.71, i.e. 1.5 times the predicted value given in Sec. III C 1. We come back below on the probable reason for this discrepancy. Despite a large experimental scatter and this slight discrepancy, we can say that in the $Bo \ll 1$ regime and for small amplitude deformations, the characteristic

timescale of the motion of the hump obeys to the linear model of overdamped relaxation developed in Sec. III.

Nevertheless, we must note that this method suffers from a major drawback. Since we use near-critical interfaces, the refractive index contrast between the two phases at coexistence is intrinsically weak. Interfaces are thick and weakly contrasted, making the detection of interface profiles difficult. This drawback is enhanced by the fact that we must use a long working distance microscope objective to observe the interface, due to the presence of an oven around the cell containing the sample. Consequently, the resulting depth of field is quite large, reducing the optical resolution. This, and the usual sensitivity of near-critical fluids properties to any thermal and composition gradients, probably explain the scattering of the data.

4. *Hump curvature dynamics*

In order to get more reliable results, we extended to liquid-liquid interfaces a method used to quantitatively characterize laser beam self-focusing in nonlinear media [29], and more recently to measure surface tension at liquid free surfaces [27].

The experimental setup used to measure the dynamics of the interface hump curvature is shown in Fig. 8. It consists in measuring the power of the laser beam refracted by the liquid interface and transmitted through a diaphragm of diameter smaller than that of the beam. The laser beam is mechanically chopped with a period of 4s in such a manner that the illumination of the sample is steady after a very short transient of $4\mu s$. The time-dependent, bell-shaped deformation induced at the interface by this upward incident beam acts as a convergent lens that focuses the beam. The focused beam emerging from the sample cell is filtered spatially using an iris diaphragm placed between the sample cell and the focus of the refracted beam. The power of this filtered beam is measured as a function of time using a photon counter and a SR430 Multi-Channel analyzer. Thus, the characteristic timescales of the dynamics of the measured optical power are similar to those of the interface deformation dynamics. For interface deformations of curvature small enough so that the resulting focal length of the liquid lens is large compared to the path of the focused beam, the power of the filtered beam is actually proportional to the hump curvature, as shown in Appendix A.

We measured the power detected by the photon counter versus time during the deforma-

tion of the interface in the temperature range $T - T_c = 2 - 20K$ and in the range of beam waist $3.47 - 31.2\mu m$, corresponding to a range of Bo number $10^{-2} - 1.8$. A typical temporal evolution of the filtered beam power is shown in the Inset of Fig. 9. For interface deformations of small amplitude, the power signal exhibits a monotonous, relaxation behavior from an initial value at the beginning of the irradiation, corresponding to the flat interface, to an asymptotic value, corresponding to the steady, bell-shaped interface acting as a lens. This confirms that the dynamics of the interface deformation is always overdamped, as predicted in Section III for the present experimental conditions. This relaxation behavior is also satisfactorily described using a single exponential relaxation of characteristic time τ_{eff} , as shown in the Inset of Fig. 9. As for the measurements of the hump height dynamics, for each measurement of τ_{eff} we checked its independence with respect to the beam power by varying P over a chosen range.

Since the scaling law $\tau_{\text{eff}} \simeq 0.5\tau(\omega_0^{-1})$ was theoretically shown to hold up to $Bo \simeq 1$ in the case of the hump curvature dynamics, we plotted in Fig. 9 the variation versus $\tau(\omega_0^{-1})$ of the characteristic timescale of evolution of the hump curvature τ_{eff} , measured for the whole range of Bo , together with its best linear fit of slope 0.98. Again, a discrepancy by a factor 2 is found between the theoretical and the experimental slopes. This could be attributed to the uncertainty on the value of $\langle \eta \rangle$. Despite this slight discrepancy, we can say that in the $Bo \ll 1$ and $Bo \simeq 1$ regimes, the characteristic timescale of the dynamics of the hump curvature obeys to the linear model of overdamped relaxation developed in Sec. III.

To summarize this Section, we showed that, given the conditions of our experiment, the dynamics of the interface deformation induced by the electromagnetic radiation pressure is overdamped, i.e. it has a relaxation behavior of characteristic timescale τ_{eff} of the order of a few tens of milliseconds. We showed experimentally that, concerning both the hump height and the hump curvature dynamics, τ_{eff} accurately obeys to a linear theory of interface deformation by a Gaussian cw laser beam. Finally, we showed numerically that, using $k = \omega_0^{-1}$ as effective wave number, the linear dispersion relation of plane interfacial waves Eq. (7) satisfactorily describes the hump curvature dynamics, whereas it fails in the $Bo \ll 1$ regime in the case of the hump height dynamics.

V. INTERFACE DYNAMICS AT THE ONSET OF THE OPTO-HYDRODYNAMIC INSTABILITY

In Ref. [30] and in the preceding companion article [12], we showed that above a given beam power threshold P_{\uparrow} , the interface becomes unstable and forms a long cylinder emitting drops, of very large aspect ratio [31], called hereafter a jet. The existence of the jet is hysteretic, i.e. after its formation at $P \geq P_{\uparrow}$, the jet persists when P is decreased until a second threshold P_{\downarrow} [32]. In order to enlighten the instability mechanism, we now study the dynamics of the interface at instability onset.

A. Experimental procedure

To study the influence of the control parameter P of the interface instability on its dynamics just beyond the threshold, we captured the motion of the unstable interface using the high-speed video camera acquiring at a rate of 250 fps. A typical series of pictures of the moving interface above instability threshold is shown in Fig. 10. The interface dynamics was analyzed as a function of both temperature, in the range $T - T_c = 2 - 10K$, and laser beam power for a fixed beam waist $\omega_0 = 3.74\mu m$, so that the dimensionless distance to the threshold $\Delta P^* = (P - P_{\uparrow})/P_{\uparrow}$ was varied in the range $0 - 1.6$. Once the temperature and the beam power are chosen, the experiment proceeds as follows. At $t = 0$, the beam shutter is set off, the laser beam suddenly impinges the interface with a power larger than P_{\uparrow} , and the interface motion is captured up to the exit of the interface tip from the camera field. We stress the fact that, because of experimental constraints, this procedure differs from classical experiments dedicated to the slow dynamics of instabilities at their onset (see e.g. ref. [33]), for which the control parameter is suddenly increased from a value just below the instability threshold to a slightly unstable value.

B. Slowing-down near the instability threshold

1. Hump height dynamics

In Figure 11a the temporal evolutions of the hump height $h(0, t)$ at $T - T_c = 8K$ are plotted for several values of beam power P , the smallest one below threshold $P_{\uparrow} = 760mW$

($\Delta P^* < 0$), the larger ones above it ($\Delta P^* > 0$). For $\Delta P^* < 0$, $h(0, t)$ exhibits a relaxation behavior of characteristic timescale τ_{eff} , similar to the linear dynamics studied in Sec. IV. On the other hand, for $\Delta P^* > 0$ each $h(0, t)$ curve exhibits an inflexion point at a hump height h_i which increases with P , and at a time t_i , called hereafter inflexion time, which decreases when P increases. The instability appears to set on at the inflexion of $h(0, t)$, although it may have begun earlier. The variations of the inflexion time t_i normalized by τ_{eff} versus ΔP^* are plotted in Figure 12 in logarithmic scales for several values of $T - T_c$. These variations range over more than a decade and are compatible with a power law behavior with exponents close to -0.65 .

2. Model of subcritical instability

The hysteresis of the hump-jet transition [32] (an example is illustrated in Fig. 13) as well as a former analysis of the bistable shape of ferrofluid drops under magnetic field [33] leads to suppose that at $P = P_\uparrow$ the hump becomes unstable and turns to a more elongated shape, the jet. At this power threshold, the sum of the electromagnetic energy and of the interfacial energy associated to the hump shape is no more a minimum, but becomes a maximum. Thus, the diagram of stability of the hump in the (h, P) plane ($h = h(0, \infty)$) should predict (i) the linear increase of h with P at small beam powers (static linear regime), (ii) a relaxation dynamics below the threshold of instability, (iii) the coexistence of two static equilibrium shapes for the hump in a given range of power below P_\uparrow , namely the small hump and the jet. The stability diagram associated to the first order, nonlinear equation

$$\frac{d\tilde{h}}{d\tilde{t}} = \tilde{P} - \tilde{h} + b\tilde{h}^2 - c\tilde{h}^3 \quad (14)$$

with $\sqrt{3c} < b < \sqrt{4c}$, qualitatively fulfills the above listed requirements. Eq. (14) involves dimensionless variables, among them a time normalized with the timescale τ_{eff} of the linear dynamics, i.e. $h(\tilde{t}) = h(0, t/\tau_{\text{eff}})$. It is similar to the hysteretic magnetization diagram of a single domain under an applied static magnetic field (imperfect sub-critical instability [34]). The stability diagram associated to Eq. 14 with $c = 0.1$ and $b = 0.6$ is shown in the Inset of Fig. 14. The hump becomes unstable at $(\tilde{h}_\uparrow, \tilde{P}_\uparrow)$. Note that close to \tilde{P}_\uparrow , \tilde{h} strongly increases, as experimentally observed in Fig. 1.

We now aim to check if Eq. (14) qualitatively reproduces the observed hump height

dynamics shown in Fig. 11a. To agree with the experimental conditions presented in Sec. V A, we computed the solutions of Eq. (14) with $\tilde{h}(0) = 0$ as a function of the initial value of the static beam power P . A relaxation of $\tilde{h}(\tilde{t})$ is observed for $\Delta P^* < 0$, while a divergent behavior very similar to Fig. 11a is observed for $\Delta P^* > 0$ (at longer times, $\tilde{h}(\tilde{t})$ converges to the upper stable branch of the stability diagram shown in the Inset of Fig. 14). Finally, the variation versus ΔP^* of the computed normalized inflexion time t_i/τ_{eff} is compared to the experimental one in Fig. 12. Excellent agreement is found, which confirms the validity over a large range in P of the phenomenological, simple nonlinear model for this instability represented by Eq. (14).

Very close to the instability threshold, the exponent of the effective power law representing the variation of t_i/τ_{eff} versus ΔP^* drops to -0.5 . This value is identical to the analytical prediction and its experimental verification by Bacri and Salin [33] of the timescale of divergence for the eccentricity of ferrofluid drops under magnetic field above instability threshold, when the magnetic field is first established at a value slightly lower than the threshold (initially motionless interface). As a matter of fact, in the present experiment, for $0 < \Delta P^* \ll 1$, the hump is almost motionless when the instability sets on.

The main difference between this model and measurements is that inflection is experimentally found to occur at a hump height h_i that depends on ΔP^* , whereas the first order differential equation (14) imposes that $d^2\tilde{h}/d\tilde{t}^2 = 0$ at \tilde{h}_\uparrow , which does not depend on ΔP^* . This discrepancy can be probably ascribed to the fact that the actual interface dynamics is not simply of first order in time, but of overdamped second order.

C. Maximum angle of incidence at inflection of $h(0, t)$

In Ref. [30], we proposed an instability mechanism based on the hypothesis that the instability occurs when the maximum of the angle of incidence along the deformed interface $\theta_{i \text{ max}}$ reaches the angle of total reflection θ_{RT} . This leads to the reflection of the whole incident electromagnetic energy towards the tip of the deformation and consequently to a huge increase of the radiation pressure acting on it. We showed in [12] that the instability mechanism should be more complex than expected, since at the instability onset the actual value of $\theta_{i \text{ max}}$ is smaller than θ_{RT} . In this section, we test whether the interface dynamics at onset is compatible, at least qualitatively, with the proposed model of instability.

We analyzed the unsteady interface shapes with the same technique as for steady ones in the preceding companion article (see section IV D of Ref. [12]). We determined the maximum value of the angle of incidence along the interface $\theta_{i \max}$ as a function of time for several temperatures in the range $T - T_c = 2 - 10K$ and several values of power P at a fixed waist $\omega_0 = 3.74\mu m$. The $\theta_{i \max}(t)$ curves obtained for several values of P above the threshold P_{\dagger} ($\Delta P^* > 0$) at $T - T_c = 8K$ are plotted in Figure 11b. $\theta_{i \max}(t)$ is found to be a monotonous function of t up to its maximum 90° . From these data, we plotted in Figure 15 the value of $\theta_{i \max}$ at time t_i of inflection of $h(0, t)$ as a function of ΔP^* for several values of $T - T_c$, together with the corresponding values of θ_{RT} . $\theta_{i \max}(t_i)$ is found to increase with ΔP^* from roughly 70° at $\Delta P^* \simeq 0$ up to values roughly equal to θ_{RT} at large values of ΔP^* , and undoubtedly smaller than 90° . Note that 70° coincides with the value of $\theta_{i \max}$ along static interfaces just below the instability threshold (see section IV D of Ref. [12]). Consequently, there is no singular change of the shape of the interface when the instability threshold is reached.

Interpreting the increase of $\theta_{i \max}(t_i)$ with ΔP^* in the frame of the reflection induced instability model, and considering Fig. 7 of the preceding companion article [12], we note that the instantaneous amount of incident light that is reflected towards the interface tip at time t_i increases strongly with ΔP^* . If the light that is partially reflected toward the interface tip is actually involved in the instability mechanism, the larger $\theta_{i \max}(t_i)$, the faster the instability should grow. Thus, the increase of $\theta_{i \max}(t_i)$ with ΔP^* , observed in Fig. 15, is compatible with the observed increase of the growth rate of the instability with ΔP^* , observed in Fig. 11a.

Finally, the fact that the maximum of $\theta_{i \max}(t_i)$ is found in Fig. 15 to be roughly equal to θ_{RT} can be explained by the following argument. When $\theta_{i \max} = \theta_{RT}$, both the radiation pressure due to the incident light [35] and the amount of light reflected toward the tip are maximum (total reflection), whatever the light polarization. Thus, when $\theta_{i \max} = \theta_{RT}$, the interface dynamics is the fastest, as observed in Fig. 11a.

To conclude this section, we showed that the instability growth rate at time t_i of apparent instability onset is linked to the value of the maximum of the angle of incidence along the deformed interface $\theta_{i \max}(t_i)$, i.e. to the amount of light reflected on the interface. This is compatible with the hypothesis that the light reflected toward the hump tip is involved in the instability mechanism.

VI. CONCLUSION

We investigated the dynamics of a liquid-liquid interface when it is deformed by the radiation pressure of a cw focused gaussian laser beam. We measured the temporal evolution of both the hump height and the hump curvature. Extending the results of ref. [10] to the case of liquid-liquid interfaces and to the $Bo \simeq 1$ regime, we showed that, in the $Bo \ll 1$ and $Bo \simeq 1$ ranges, the temporal evolution of the small amplitude deformations is correctly described by a linear hydrodynamic theory predicting an overdamped dynamics. In particular, the dynamics of the hump curvature is accurately predicted by the dispersion relation of plane interfacial waves Eq. (7) using $k_{\text{eff}} = 0.5\omega_0^{-1}$ as the effective wave number representing the hump deformation up to $Bo \simeq 1$. Surprisingly, we showed numerically this is not the case for the dynamics of the hump height at $Bo \ll 1$. We also investigated the dynamics of the large amplitude interface deformations at the onset of the opto-hydrodynamic instability. Using a simple, phenomenological model for the nonlinear evolution of the hump height, we interpreted the observed interface dynamics at the instability onset as the signature of an imperfect subcritical instability. Nevertheless, the actual instability mechanism remains unrevealed by the theory and shall deserve further investigation.

Acknowledgments

The authors thank S. Fauve for fruitful discussion and A. Chater for his experimental contribution. They also thank M. Winckert and J. Plantard for technical assistance. This work was partly supported by Centre National de la Recherche Scientifique and Conseil Régional d'Aquitaine.

APPENDIX A: RELATIONSHIP BETWEEN THE CURVATURE OF THE HUMP AND THE INTENSITY OF THE TRANSMITTED LIGHT

The determination of the hump curvature dynamics is based on the measurement of the temporal evolution of the intensity of the laser beam refracted by the hump acting as a lens. To be able to compare our beam power measurements to the predicted characteristic timescale of evolution of the hump curvature, the beam power variations have to be proportional to the hump curvature variations. In this appendix, we prove that it is effectively

the case for interface deformations of curvature small enough so that the resulting focal length of the liquid lens is large compared to the path of the focused beam. The detailed optical setup used to filter and measure the beam transmitted through the hump is shown in Fig. 16. Taking into account the smallness of the beam waists used, it is not possible to directly measure the optical transmission through a diaphragm located just behind the sample. Thus, we used the microscope objective $O2$ to image the exit face of the sample cell on the iris diaphragm located at a large distance, as shown in Fig. 16. If P_i denotes the power of the TEM_{00} Gaussian beam incident to the diaphragm and P_t the transmitted beam power, the transfer function T of the diaphragm of aperture radius ρ is given by

$$T = \frac{P_t}{P_i} = 1 - \exp\left(-2\frac{\rho^2}{\omega'^2}\right), \quad (\text{A1})$$

where ω' is the beam radius on the diaphragm. Since the distance p' between $O2$ and the iris diaphragm is large compared to the distance p between the exit face of the experimental cell and $O2$, we can approximate the gaussian propagation laws by those of geometric optics. Then, $\omega'/\omega = p'/p$, where $\omega(z)$ is the beam radius at the exit face of the experimental cell; in our experiment, we have $z = 2mm$ corresponding to $1mm$ of phase Φ_2 plus $1mm$ of quartz window. The transfer function becomes:

$$T = 1 - \exp\left(-2\frac{\rho^2}{(p'/p)^2\omega^2}\right), \quad (\text{A2})$$

Without any focusing effect (flat interface), the beam radius $\omega(z)_{f=\infty}$ at the exit face of the sample cell is such that

$$\omega(z)_{f=\infty}^2 = \omega_0^2 \left(1 + \left(\frac{\lambda z}{\pi\omega_0^2}\right)^2\right), \quad (\text{A3})$$

in the paraxial ray approximation, where ω_0 is the beam waist at the interface ($z = 0$). Besides, when the interface is deformed and gives birth to a thin lens of focal distance f , the expression of the beam radius $\omega(z)_f$ at the exit face of the cell is:

$$\omega(z)_f^2 = \omega_0^2 \left(\left(1 - \frac{z}{f}\right)^2 + \left(\frac{\lambda z}{\pi\omega_0^2}\right)^2\right). \quad (\text{A4})$$

Experimentally, we considered a situation where $z < f$ in order to investigate the dynamics of the interface in the linear regime in deformation. Moreover, we choose $\rho/\omega' < 1$ to work in the paraxial ray approximation where the interface deformation can be assimilated to a

thin spherical lens. In these conditions, we get:

$$T(\omega(z)_f) \approx T(\omega(z)_{f=\infty}) \left(1 + 2 \left(\frac{\omega_0}{\omega(z)_{f=\infty}} \right)^2 \frac{z}{f} \right). \quad (\text{A5})$$

Note that both ω_0 and z are fixed in a given experiment, so that the only time dependent variable is f . Finally, in the paraxial ray approximation, f is given by [36]:

$$\frac{1}{f} = \frac{n_2 - n_1}{2n_2} \kappa(0, t), \quad (\text{A6})$$

where $\kappa(0, t)$ is the curvature of the interface on the beam axis at time t . This leads to:

$$T(\omega(z)_{f(t)}) \simeq T(\omega(z)_{f=\infty}) (1 + \alpha \kappa(0, t)) \quad (\text{A7})$$

where α is a constant. Consequently, the beam power transmitted through the iris diaphragm is an affine function of $\kappa(0, t)$. Assuming $\kappa(0, t) = \kappa(0, \infty)(1 - \exp(-t/\tau_{\text{eff}}))$, we finally find:

$$T(\omega(z)_{f(t)}) \simeq T(\omega(z)_{f=\infty}) (1 + \alpha \kappa(0, \infty)(1 - \exp(-t/\tau_{\text{eff}}))). \quad (\text{A8})$$

where τ_{eff} is the characteristic timescale of the linear interface deformation. The fit of the example of temporal behavior of the transmission presented in the Inset of Fig. 9 by the predicted expression Eq. (A8) shows up good agreement.

-
- [1] A. Ashkin and J.M. Dziedzic, Phys. Rev. Lett. **30**, 139 (1973).
 - [2] J. Z. Zhang and R. K. Chang, Opt. Lett. **13**, 916 (1988).
 - [3] I. I. Komissarova, G. V. Ostrovskaya, and E. N. Shedova, Optics Comm. **66**, 15 (1987).
 - [4] A. Casner and J.P. Delville, Opt. Lett. **26**, 1418 (2001).
 - [5] A. A. Kolomenskii and H. A. Schuessler, Appl. Optics **38**, 6357 (1999).
 - [6] J. P. Longtin, K. Hijikata, and K. Ogawa, Int. J. Heat Mass Transfer **42**, 85 (1999).
 - [7] J. C. Loulergue, Y. Lvy, and C. Imbert, Optics Comm. **45**, 149 (1983).
 - [8] S. A. Viznyuk, P. P. Pashinin, and A. T. Sukhodol'skii, Optics Comm. **85**, 254 (1991).
 - [9] K. Sakai, K. Tachibana, S. Mitani, and K. Takagi, J. Colloid Interface Sci **264**, 446 (2003).
 - [10] Y. Yoshitake, S. Mitani, K. Sakai, and K. Takagi, J. Appl. Phys. **97**, 024901 (2005).
 - [11] A. Casner and J.P. Delville, Phys. Rev. Lett. **87**, 054503 (2001).
 - [12] R. Wunenburger, A. Casner, and J.P. Delville, submitted to Phys. Rev. E.

- [13] H. M. Lai, P. T. Leung, K. L. Poon, and K. Young, J. Opt. Soc. Am. B **6**, 2430 (1989).
- [14] I. Brevik and R. Kluge, J. Opt. Soc. Am. B **16**, 976 (1999).
- [15] A. Hallanger, I. Brevik, S. Haaland, and R. Sollie, Phys. Rev. E **71**, 056601 (2005).
- [16] A. M. Gañan-Calvo, J. Dávila, and A. Barrero, J. Aerosol Sci. **28**, 249 (1997).
- [17] R. Badie and D. Frits de Lange, Proc. R. Soc. Lond. A **453**, 2573 (1997).
- [18] B. Jean-Jean, E. Freysz, A. Ducasse, and B. Pouligny, Europhys. Lett. **7**, 219 (1986).
- [19] G. V. Ostrovskaya, Sov. Phys. Tech. Phys. **33**, 465 (1988).
- [20] G. B. Arfken and H. J. Weber, *Mathematic methods for physicists*, 4th Ed. (Academic, New York, 1995).
- [21] V. G. Levich, *Physiochemical Hydrodynamics* (Prentice Hall, London, 1962), § 117.
- [22] H. Lamb, *Hydrodynamics*, 6th Ed. (Cambridge, 1997), Chap. XI 349.
- [23] M. S. Plesset and C. G. Whipple, Phys. Fluids **17**, 1 (1974).
- [24] J. L. Harden, H. Pleiner, and P. A. Pincus, J. Chem. Phys. **94**, 5208 (1991).
- [25] As a matter of fact, Eq. (7) can be solved analytically in its polynomial form involving the variable A , i.e. by determining the roots of the denominator of the last term of the integrand in Eq. (4).
- [26] E. Freysz, Ph. D. thesis, Bordeaux I University, 1990.
- [27] K. Sakai, D. Mizuno, and K. Takagi, Phys. Rev. E **63**, 046302 (2001).
- [28] This is linked to a classical problem of convergence of the diffusion equation in cylindrical geometry (see for instance J. P. Gordon *et al.*, J. Appl. Phys. **36**, 3 (1965)). As far as we consider a boundary condition at infinity, the gradient in height approaches $1/r$ in the steady state and with the boundary condition $h(r = \infty, t) = 0$, the height integrates to infinity at all finite radii. That is why we took a finite boundary condition ($h(r = \omega_{bc}, t = \infty)$) to find the stationary solution [12].
- [29] B. Jean-Jean, E. Freysz, A. Ponton, A. Ducasse, and B. Pouligny, Phys. Rev. A **39**, 5268 (1989).
- [30] A. Casner and J. P. Delville, Phys. Rev. Lett. **90**, 144503 (2003).
- [31] A. Casner and J. P. Delville, Europhys. Lett. **65**, 337 (2004).
- [32] unpublished results.
- [33] J. C. Bacri and D. Salin, Journal of Magnetism and Magnetic Materials **39**, 48 (1983).
- [34] P. Manneville, *Structures dissipatives chaos et turbulence* (CEA, Saclay, 1991).

- [35] A. Casner, J.P. Delville, and I. Brevik, J. Opt. Soc. Am. B **20**, 2355 (2003).
- [36] M. Born and E. Wolf, *Principles of Optics*, 6th Ed., (Pergamon, Oxford, 1980).

Captions

Figure 1: Variation of the height $h(r=0)$ of the interface deformation versus the incident beam power P when the laser propagates upward (\blacktriangle) and downward (∇). Lines are just guides for the eye. The bottom set of pictures illustrates the evolution of the deformation for an upward excitation with the emergence of a tether-like shape; from left to right: $P = 270mW$, $P = 410mW$, $P = 590mW$ and $P = 830mW$. The top set of pictures shows the evolution of the deformation for a downward excitation with the interface disruption and the formation a liquid jet which appear above the threshold power P_{\dagger} schematized by the dash-dotted line; from right to left: $P = 310mW$, $P = 370mW$, $P = P_{\dagger} = 400mW$ at instability onset and $P = 400mW$ at steady state (picture not on scale). $\omega_0 = 5.3\mu m$, $T - T_c = 3K$.

Figure 2: Variations of the reduced hump height $h^*(t) = h(0, t)/h(0, \infty)$ as a function of the reduced time $t^* = t/\tau(\omega_0^{-1})$ (defined by Eq. (10)) for several Bo values indicated nearby them. Solid lines are best exponential fits $1 - e^{-t/\tau_{\text{eff}}}$ to $h^*(t)$. Inset: (\square) Variation of the reduced characteristic timescale of evolution of $h^*(t)$, $\tau_{\text{eff}}/\tau(\omega_0^{-1})$, versus Bo . (\blacksquare) Asymptotic value of $\tau_{\text{eff}}/\tau(\omega_0^{-1})$ for $Bo \rightarrow \infty$. The solid line is a $-1/3$ power law.

Figure 3: Variations of the reduced hump curvature $\kappa^*(t) = \kappa(0, t)/\kappa(0, \infty)$ as a function of the reduced time $t^* = t/\tau(\omega_0^{-1})$ (defined by Eq. (10)) for several Bo values indicated nearby them. Solid lines are best exponential fits $1 - e^{-t/\tau_{\text{eff}}}$ to $\kappa^*(t)$. Inset: (\square) Variation of the reduced characteristic timescale of evolution of $\kappa^*(t)$, $\tau_{\text{eff}}/\tau(\omega_0^{-1})$, versus Bo . (\blacksquare) Asymptotic values of $\tau_{\text{eff}}/\tau(\omega_0^{-1})$ for $Bo \rightarrow 0$ and $Bo \rightarrow \infty$.

Figure 4: Typical temporal behavior of an interface distortion in the regime of linear deformation when the cw optical excitation is suddenly applied at time $t = 0s$. The parameters are: $P = 840mW$, $\omega_0 = 6.3\mu m$ and $T - T_c = 10K$.

Figure 5: Temporal evolution of the reduced hump height $h(0, t)/h(0, \infty)$ corresponding to the temporal evolutions of the hump height observed for various beam powers shown in the Inset. The asymptotic value $h(0, \infty)$ is determined for each P from an exponential fit of $h(0, t)$ shown in Inset.

Figure 6: Temporal behavior of the reduced hump height $h(0, t)/h(0, \infty)$ versus the beam waist ω_0 and the vicinity to the critical point $T - T_c$ (Inset). Lines are exponential fits.

Figure 7: Variation of the characteristic timescale τ_{eff} of the hump height evolution versus its predicted scaling behavior $4\langle\eta\rangle\omega_0/\sigma Bo^{-1/3}$ for several temperatures. The solid line is

the best linear fit, of slope 0.71.

Figure 8: Experimental setup used to measure the dynamics of the interface hump curvature along the beam axis. The pictures illustrate the beam focusing induced by the interface deformation for increasing beam powers (up to down).

Figure 9: Variation of the characteristic timescale τ_{eff} of the hump curvature evolution versus its predicted scaling behavior $\tau(\omega_0^{-1}) = 4\langle\eta\rangle\omega_0/\sigma$. The Solid line is the best linear fit of slope 0.98. The Bo number ranges from 10^{-2} to 1.8. Inset: Typical power signal measured by the photon counter. The sample temperature is such that $T - T_c = 15K$. The illumination by the laser beam of waist $\omega_0 = 24.5\mu m$ and power $500mW$ begins at $t = 0$. The solid line corresponds to the best fit by an exponential function of characteristic time $\tau_{\text{eff}} = 39ms$.

Figure 10: Sequential pictures of the moving interface at $T - T_c = 8K$ above the instability threshold $P_{\uparrow} = 755mW$. The laser illumination of power $P = 840mW$ and waist $\omega_0 = 3.74\mu m$ started at $t = 0$.

Figure 11: (a) Temporal evolutions of the interface hump height $h(0, t)$ at $T - T_c = 8K$ for several values of beam power P below and above threshold $P_{\uparrow} = 760mW$: (\square) $P = 700mW$. (\bullet) $P = 770mW$. (\blacksquare) $P = 840mW$. (\blacklozenge) $P = 910mW$. (\blacktriangledown) $P = 980mW$. (\blacktriangle) $P = 1120mW$. (\blacktriangleleft) $P = 1260mW$. (\blacktriangleright) $P = 1400mW$. (b) Corresponding temporal evolutions of maximum angle of incidence $\theta_{i\text{max}}(t)$ along the interface. Symbols are the same.

Figure 12: Instant t_i of inflection of $h(0, t)$ (see Fig. 11a) normalized by the characteristic timescale of relation τ_{eff} below the instability threshold, as a function of the reduced distance to the beam power threshold $\Delta P^* = (P - P_{\uparrow})/P_{\uparrow}$ for several values of $T - T_c$. The solid line is the prediction of a model of imperfect subcritical instability (see Fig. 14).

Figure 13: Hysteresis of the deformation height versus the beam power. $T - T_c = 18K$ and $\omega_0 = 3.5\mu m$. The lower branch of the hysteresis corresponds to the static hump studied in Ref. [12], whereas its upper branch corresponds to an elongated shape emitting droplets (jet).

Figure 14: Temporal evolutions of the reduced height $\tilde{h}(\tilde{t})$ ($\tilde{t} = t/\tau_{\text{eff}}$) computed for several distances to the instability threshold ΔP^* using the amplitude equation (14). τ_{eff} is the characteristic timescale of the hump linear dynamics. Inset: stability diagram associated to Eq. (14).

Figure 15: Variation of the maximum value of the angle of incidence along the interface $\theta_{i \max}$ at the time t_i corresponding to the inflection of $h(0, t)$ (see Fig. 11a) as a function of the reduced distance to onset ΔP^* for several values of $T - T_c$. Lines joining experimental data are a guide for the eye. Each horizontal line decorated with open symbols indicates the value of the angle of total reflection θ_{RT} at the temperature corresponding to the full symbols.

Figure 16: Optical setup to filter and measure the beam transmitted through the hump. $O1$ and $O2$ are the microscope lenses used respectively to focus the laser beam on the fluid interface (beam waist ω_0) and to image the beam radius ω at the exit face of the cell C on the iris diaphragm (beam waist ω'). ω'_0 is an intermediate beam waist. p (resp. p') are the distances between the exit face of the cell and $O2$ (resp. between $O2$ and the iris diaphragm).

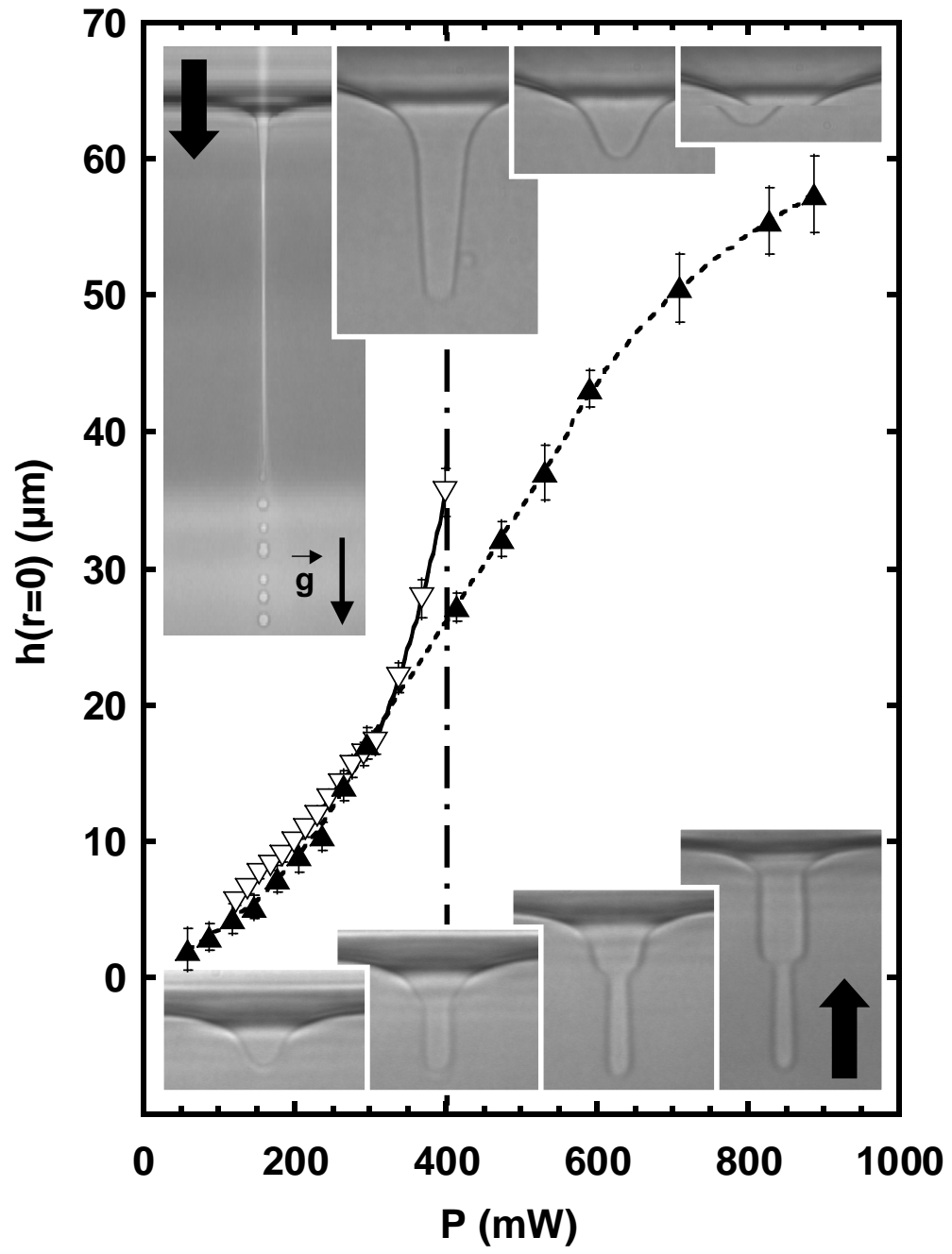


FIG. 1:

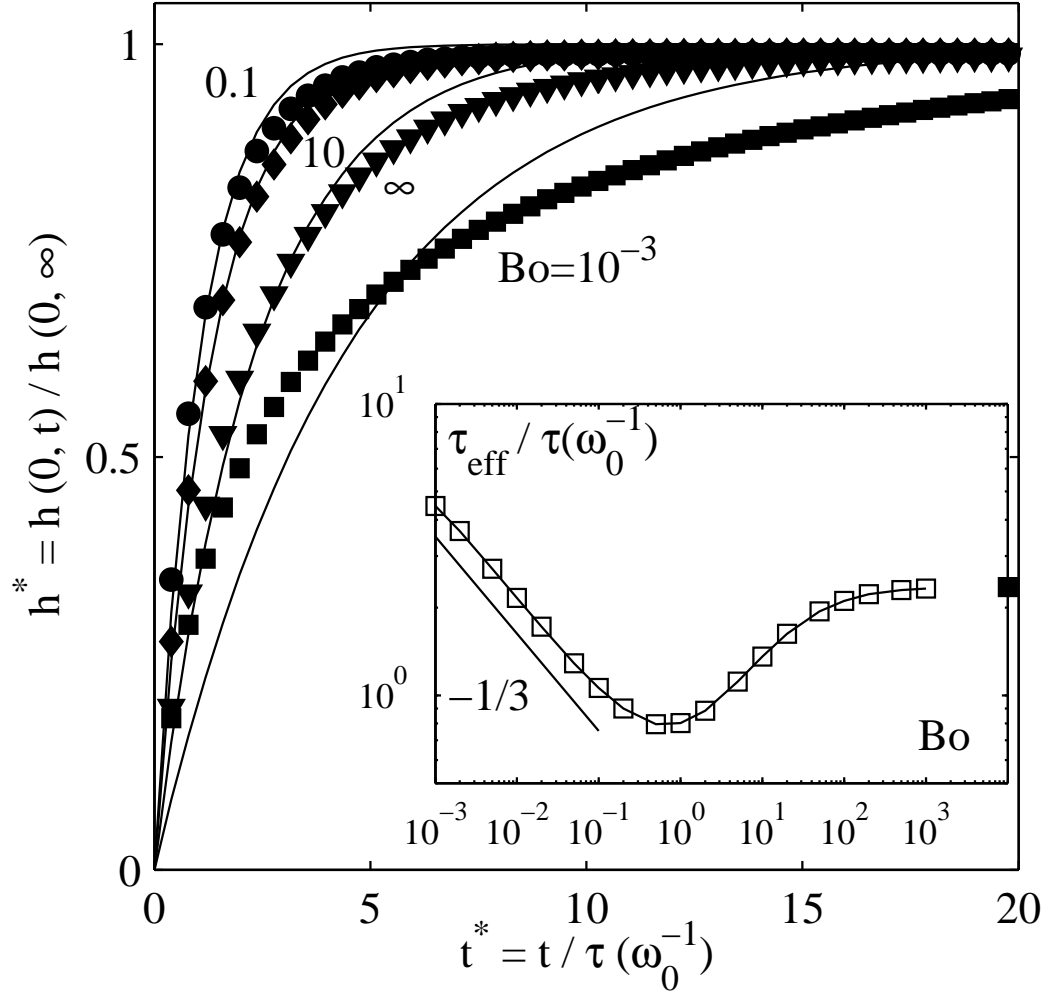


FIG. 2:

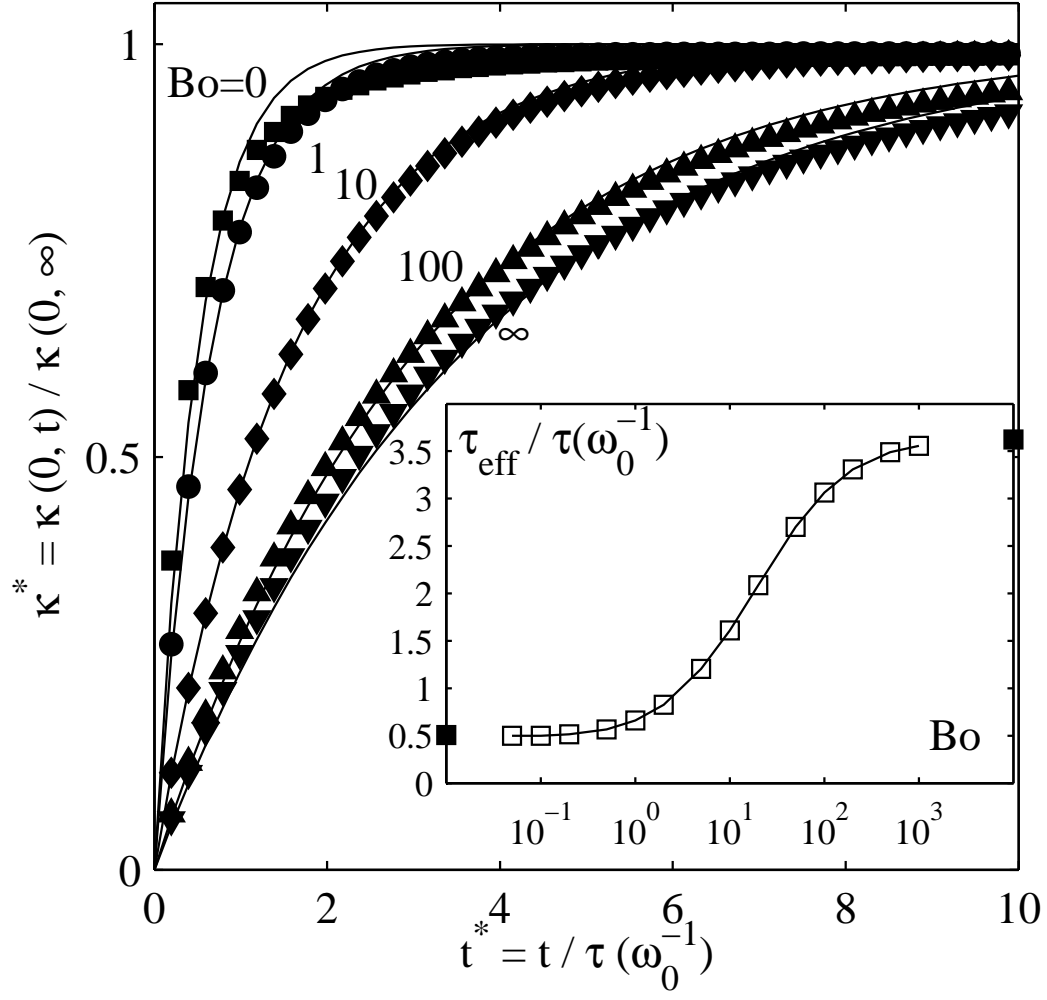


FIG. 3:

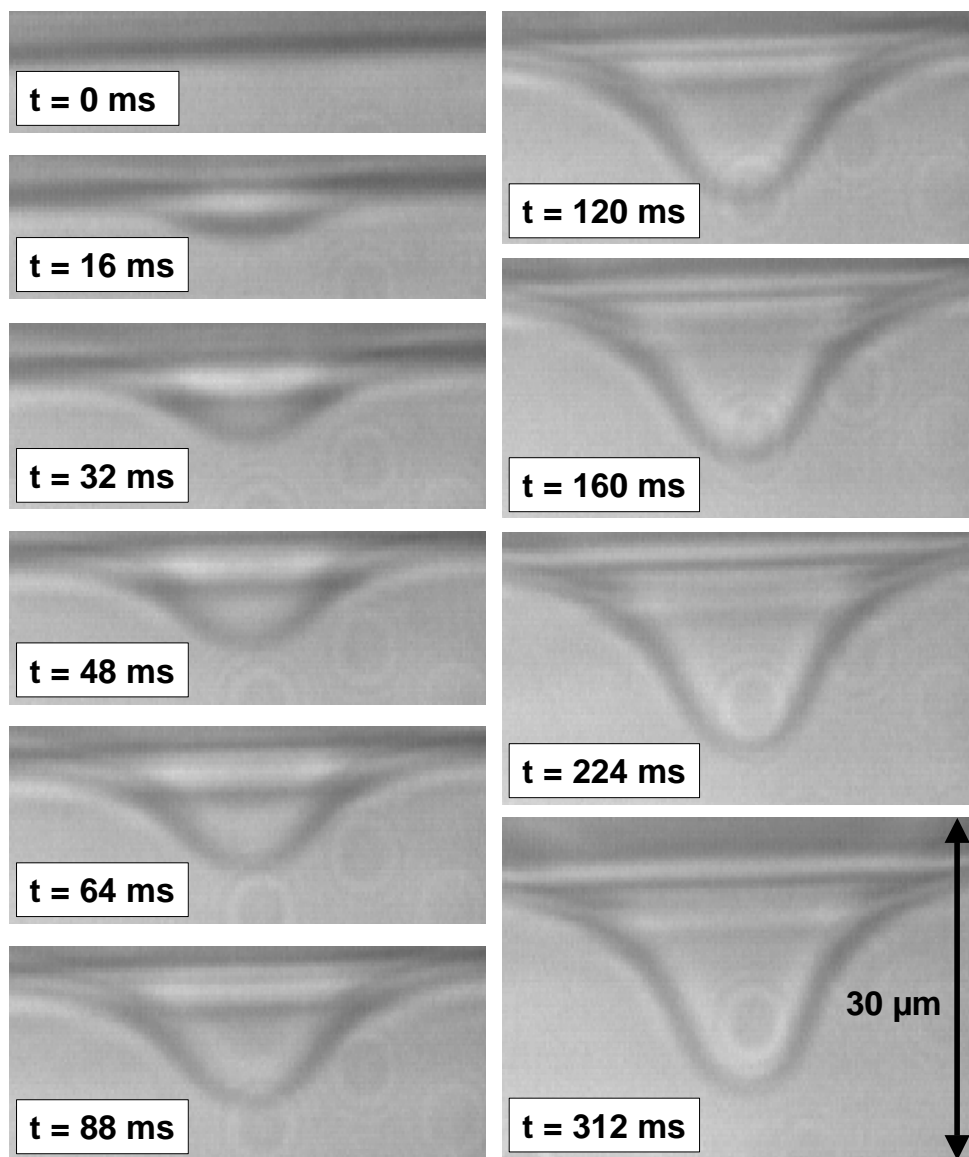


FIG. 4:

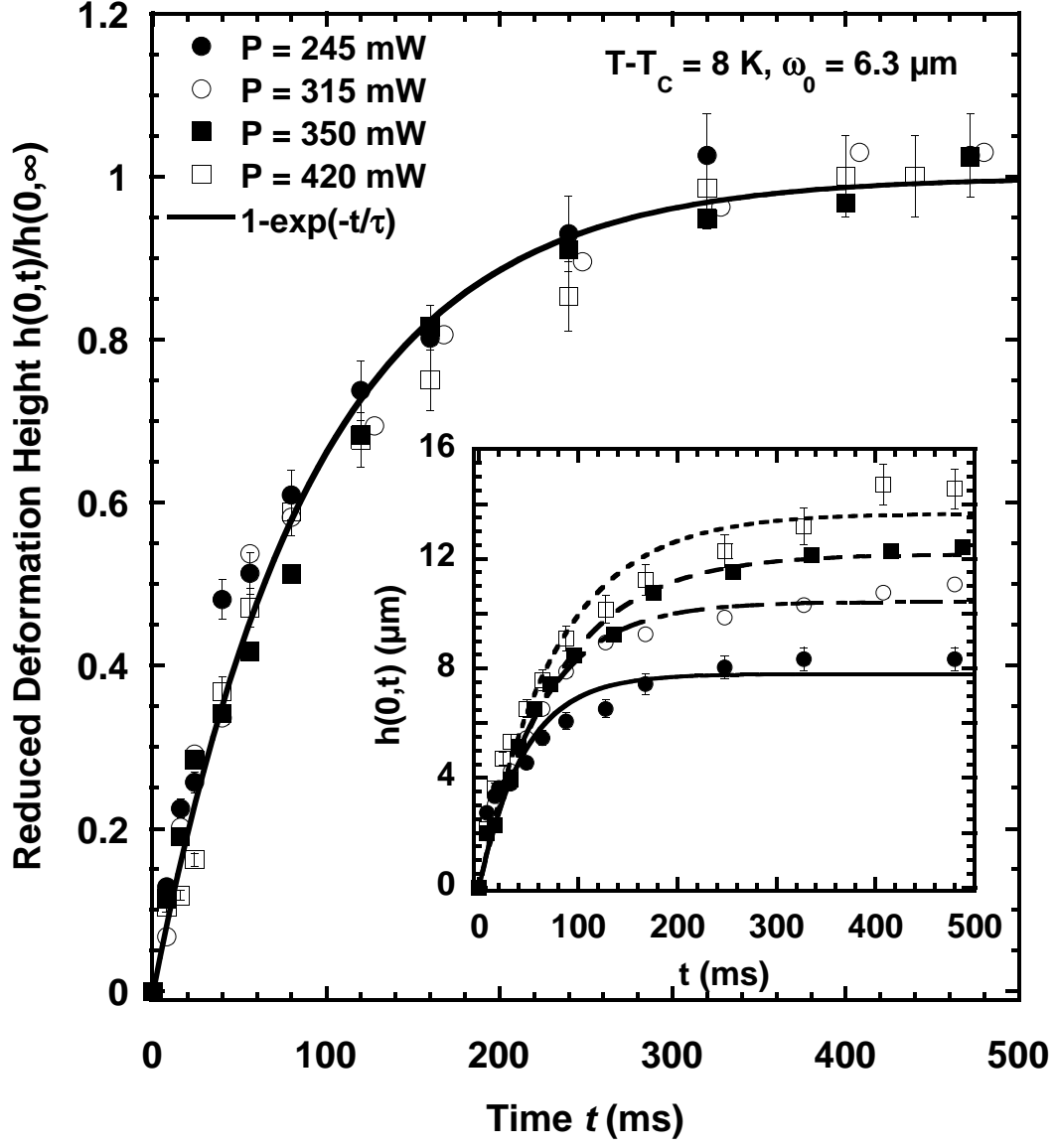


FIG. 5:

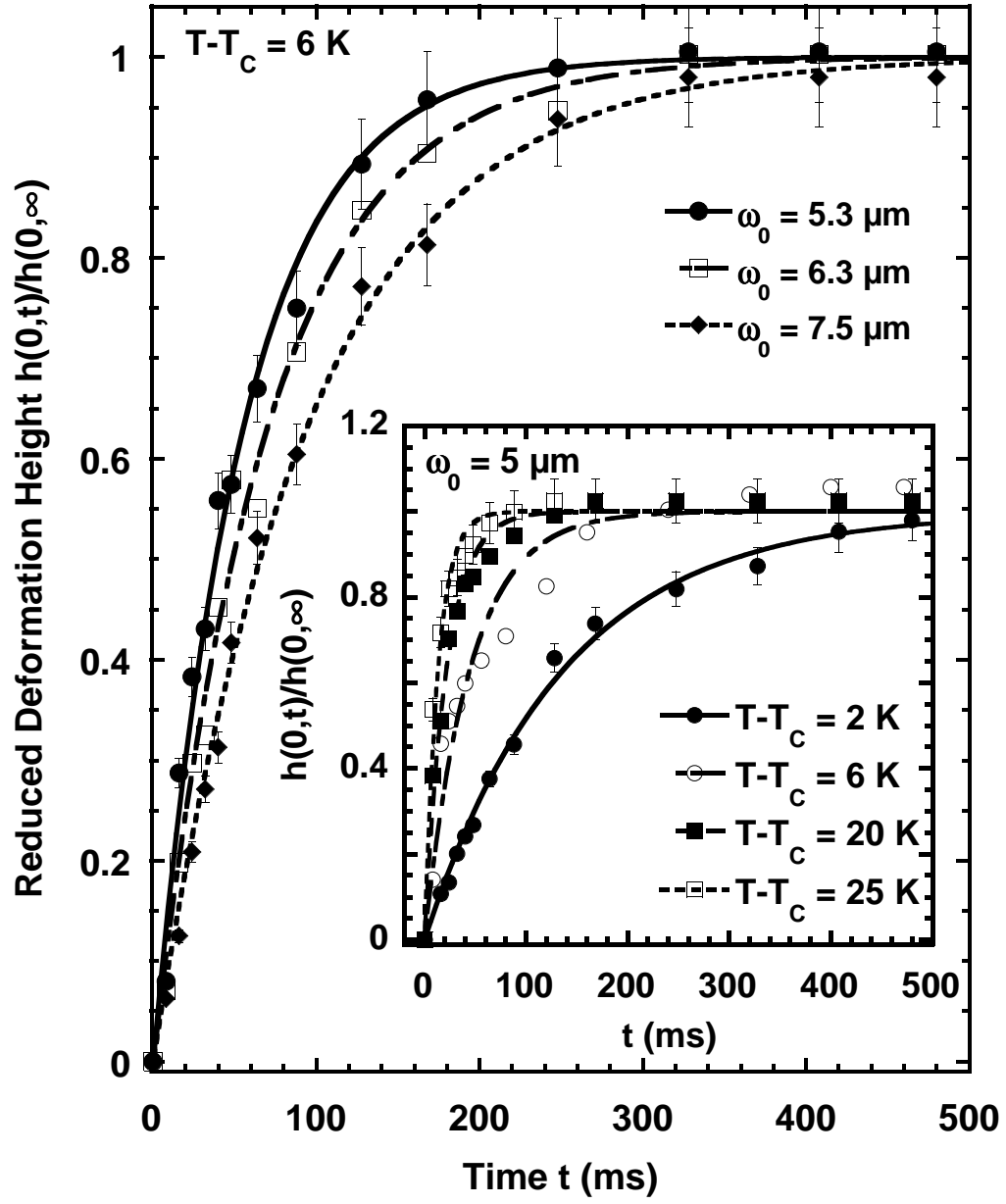


FIG. 6:

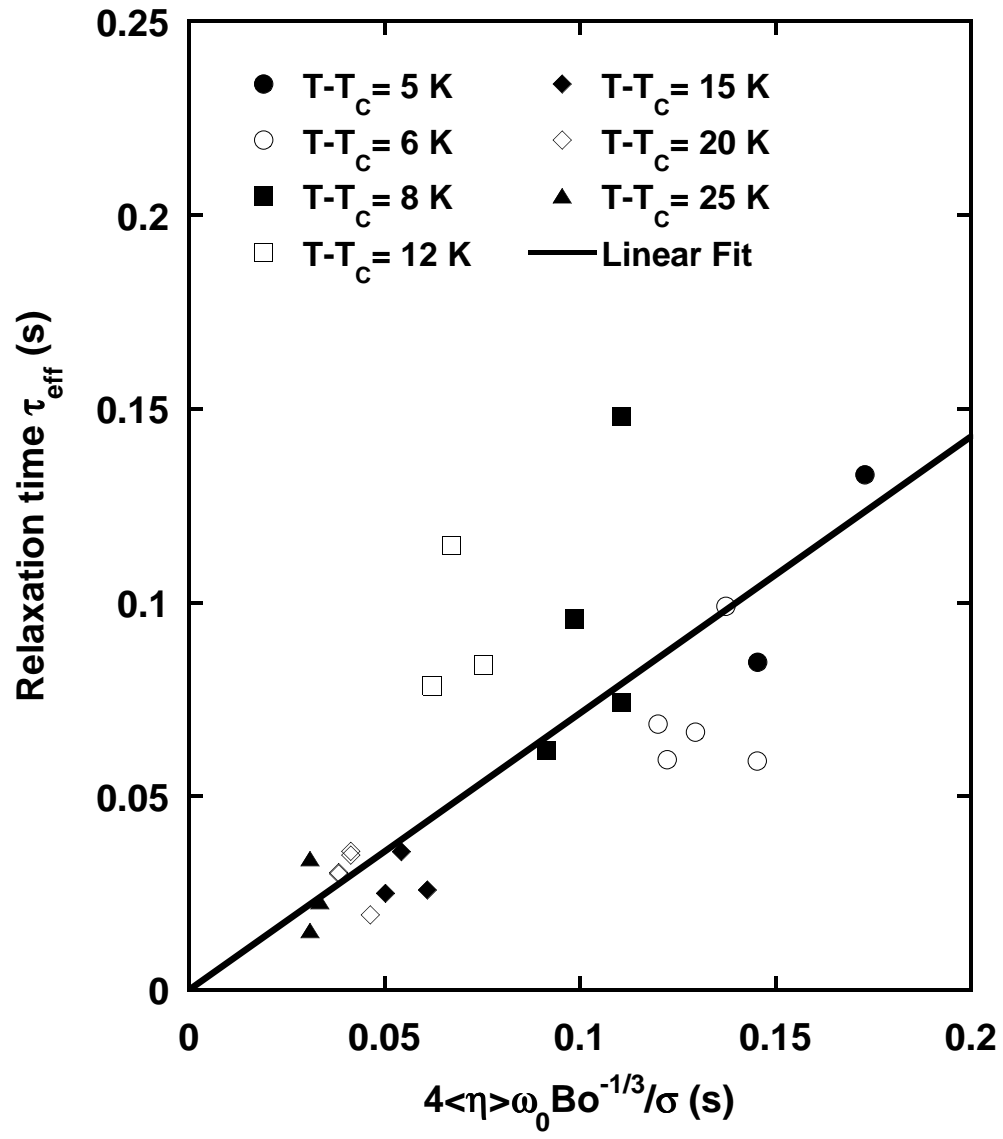


FIG. 7:

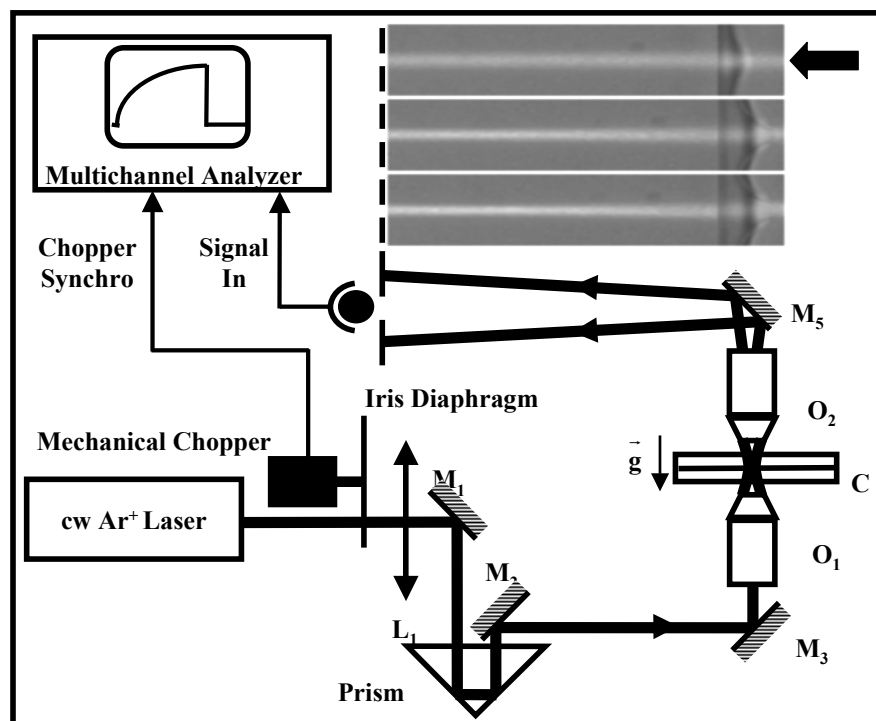


FIG. 8:

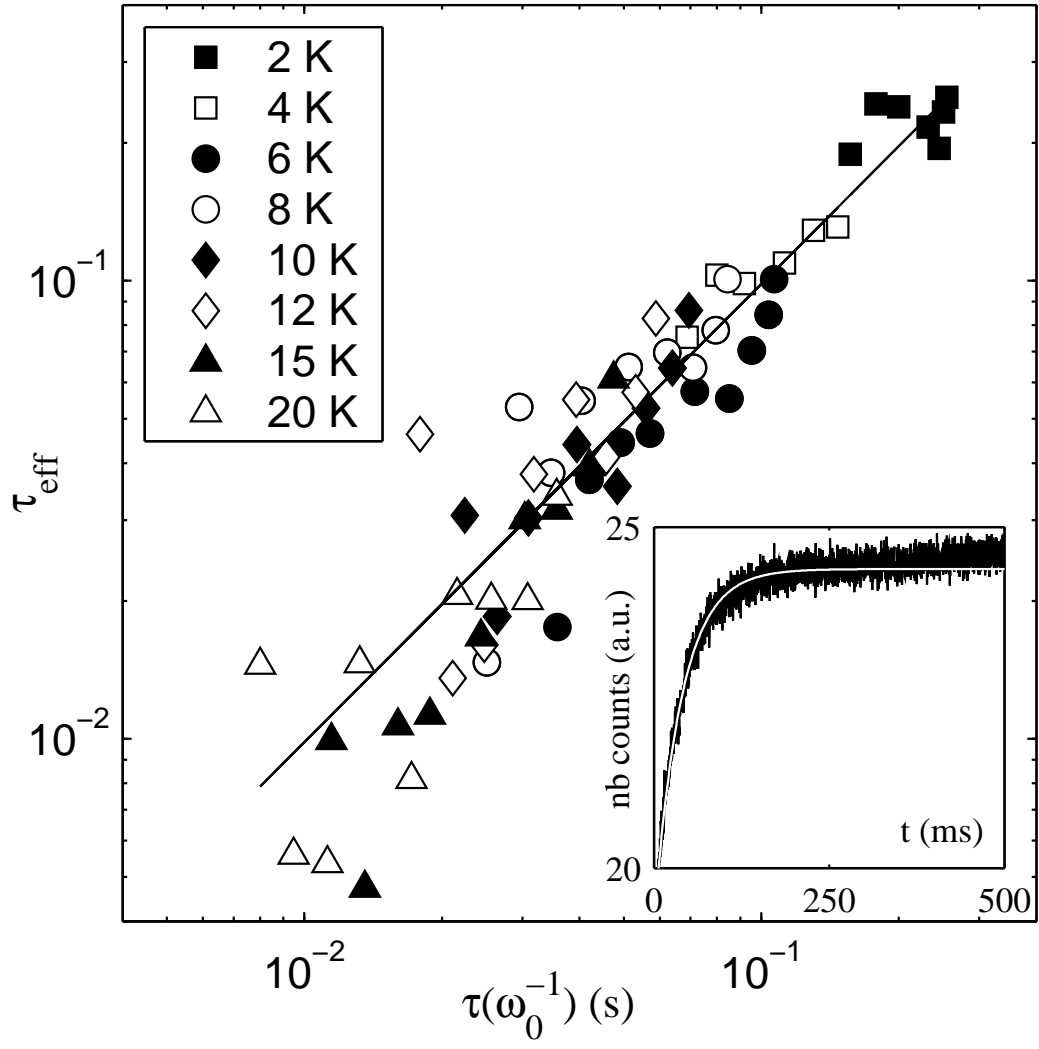


FIG. 9:

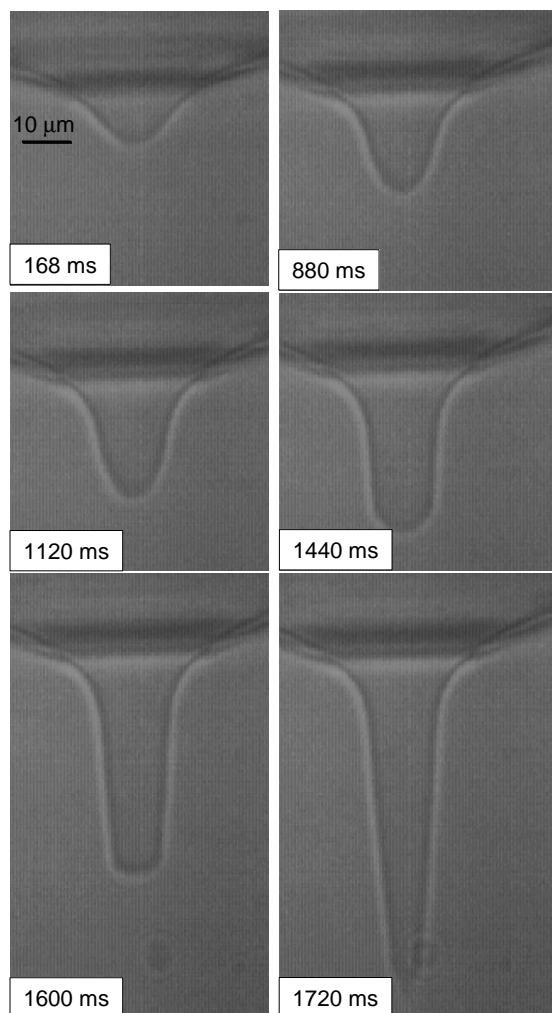


FIG. 10:

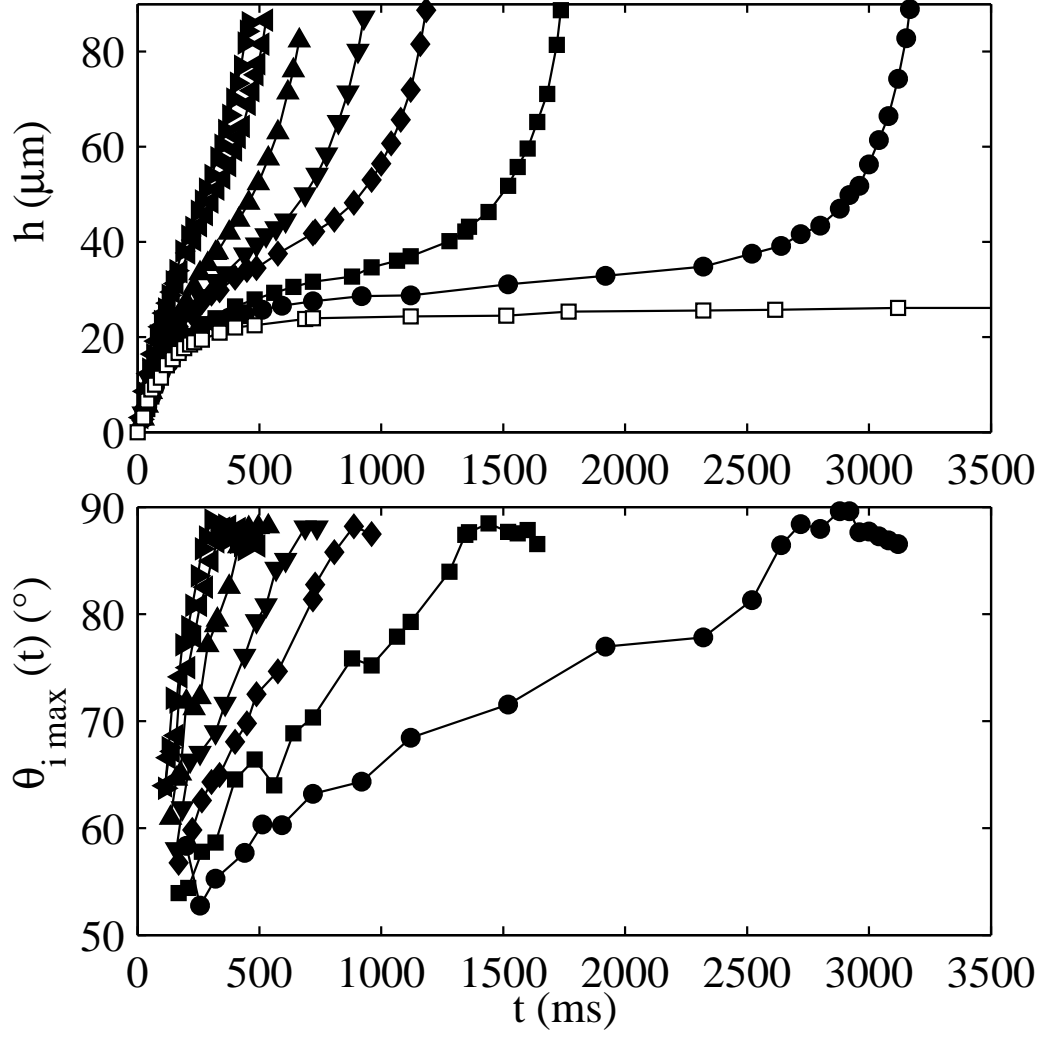


FIG. 11:

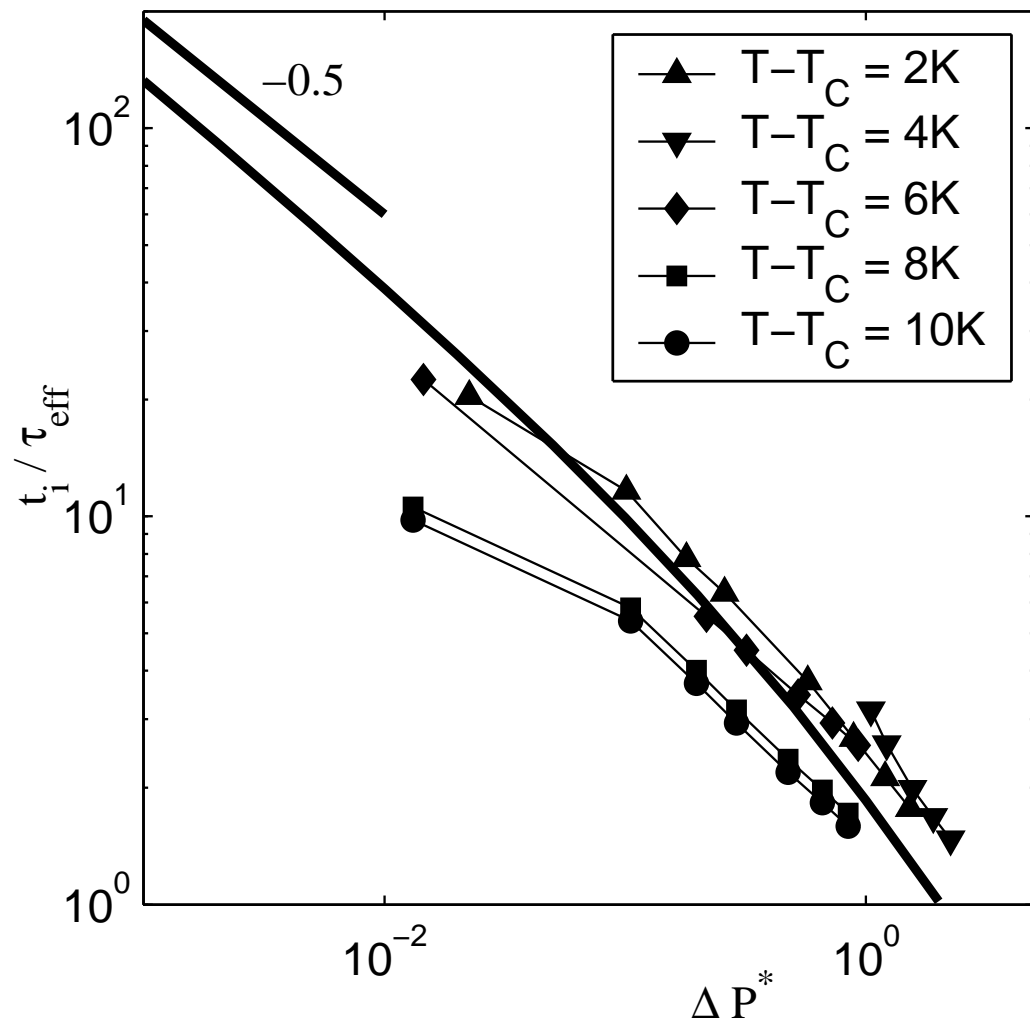


FIG. 12:

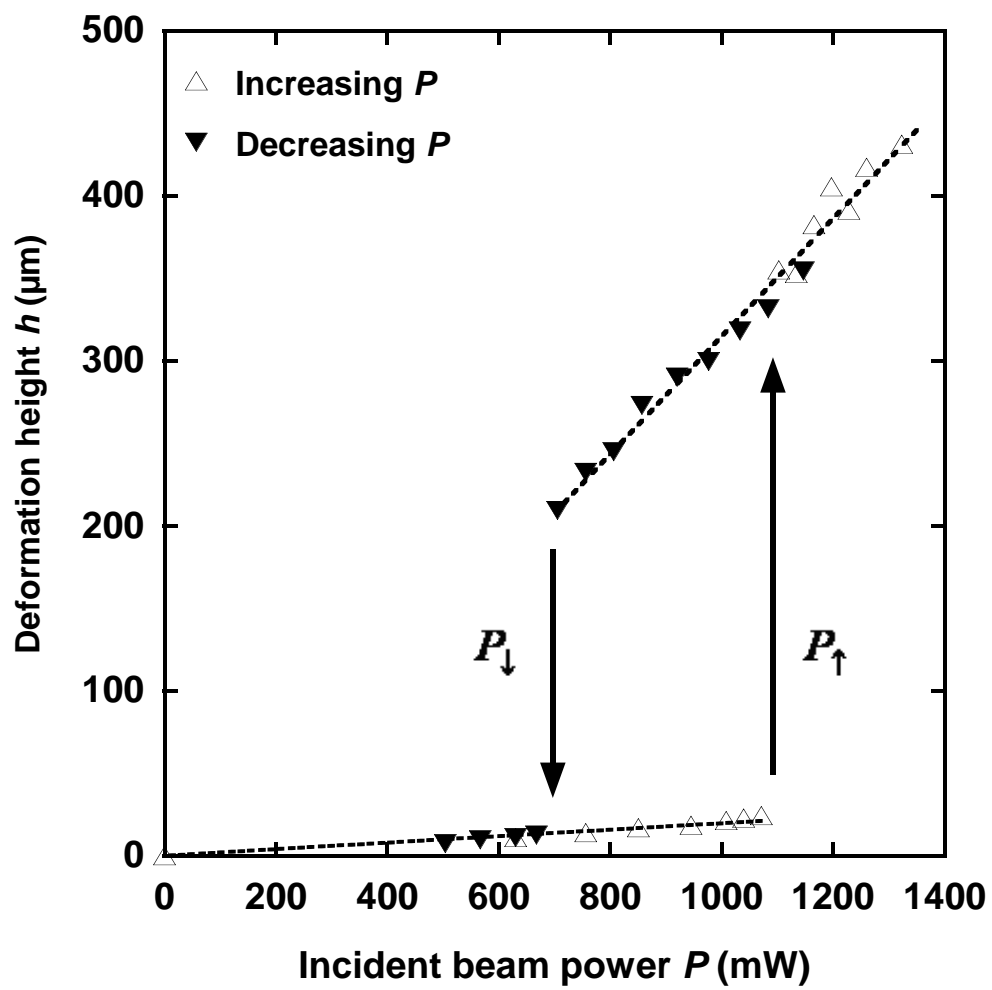


FIG. 13:

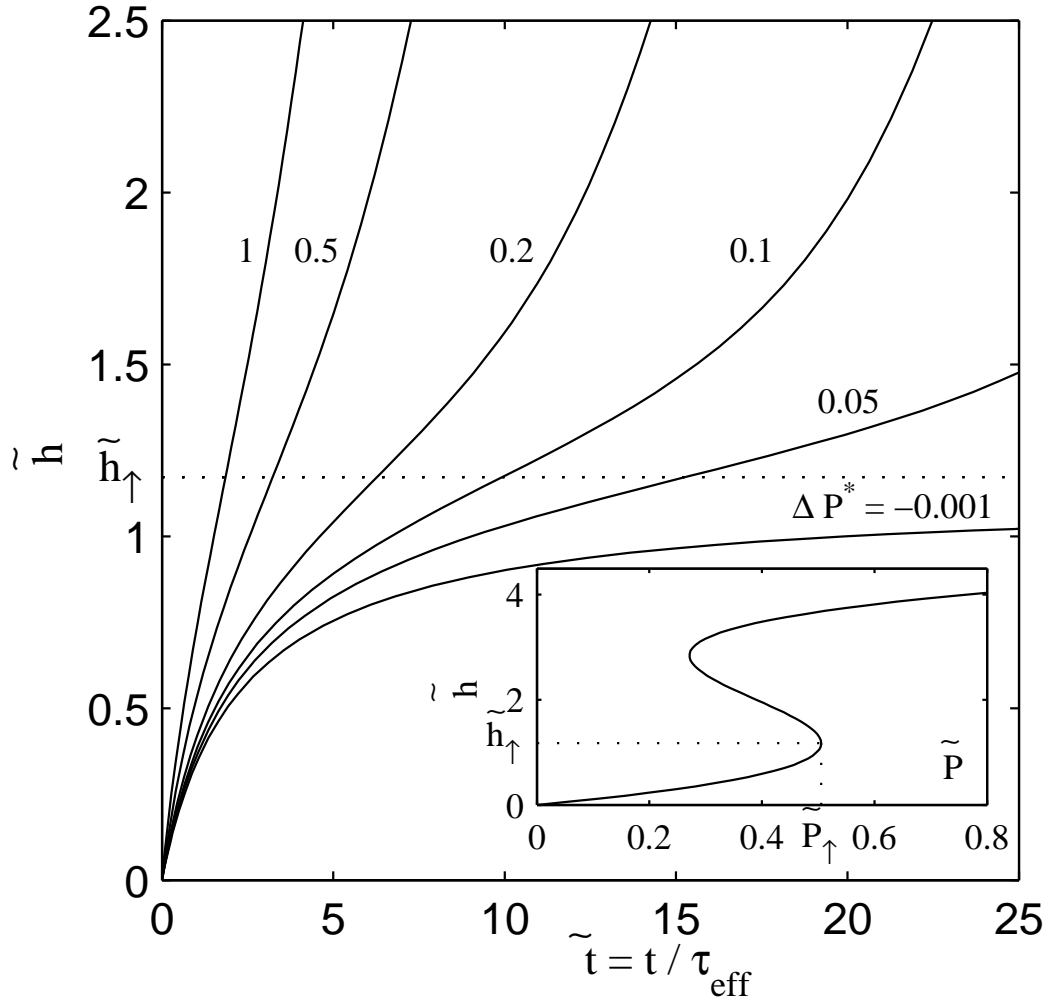


FIG. 14:

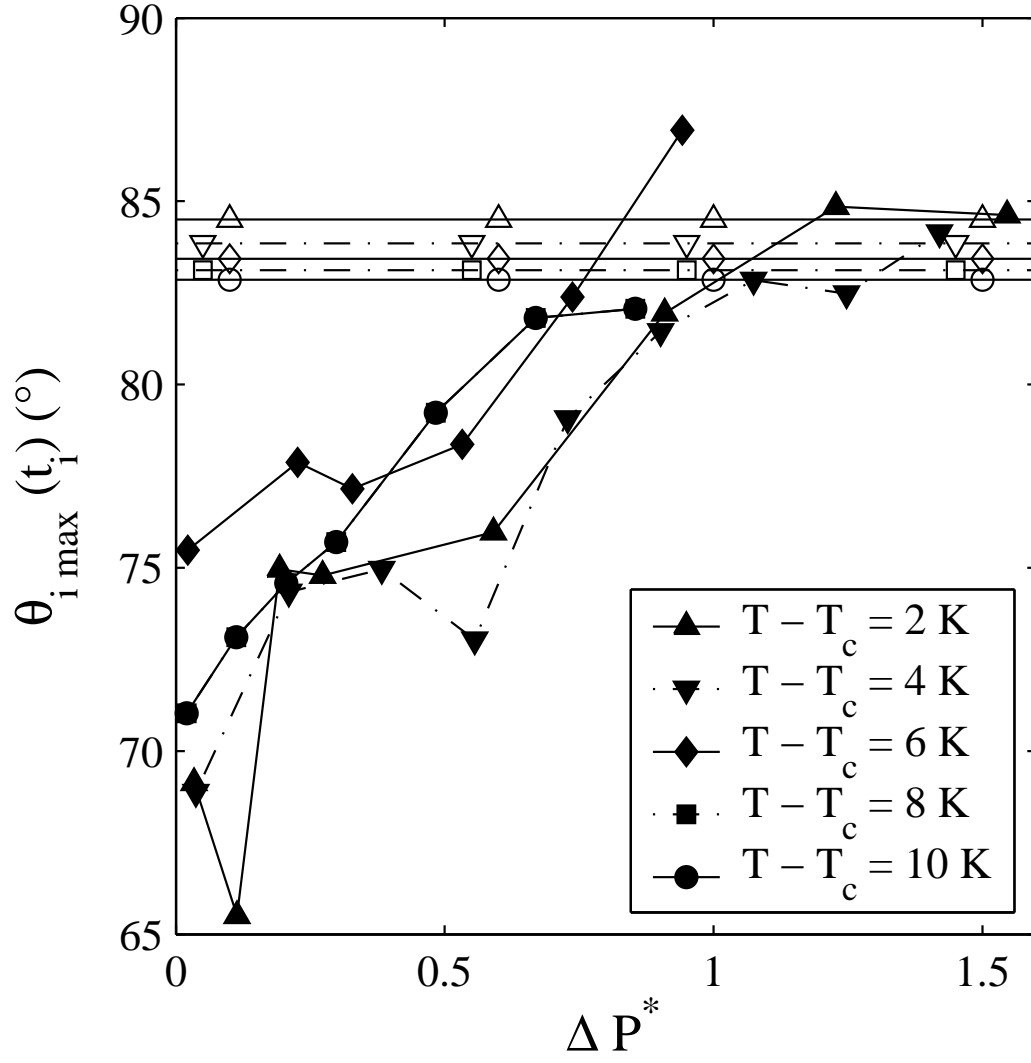


FIG. 15:

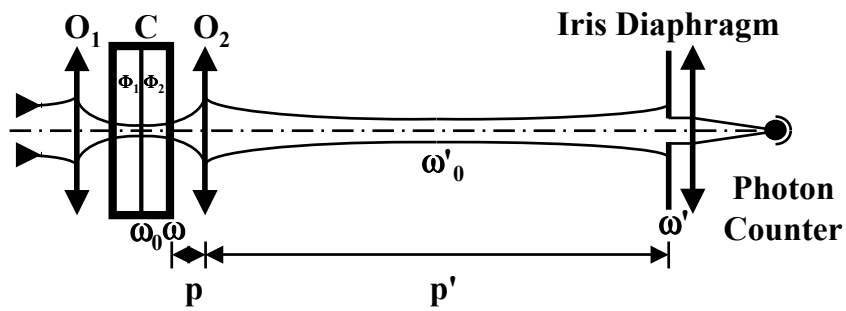


FIG. 16: